J Mater Sci: Mater Electron (2026) 37:715

Electrical and dielectric tailoring of glass fiber-reinforced concrete using ZnO-based hybrid nanocomposites

Doğu Ramazanoğlu[1,*], Ahmad Badreddin Musatat[2], Azime Subaşı[3], Ahmet Demir[4], Serkan Subaşı[5], and Muhammed Maraşlı[6]

[1] *Department of Materials Science and Nanotechnology Engineering, Faculty of Engineering, İstanbul Gedik University, Istanbul, Türkiye*
[2] *Department of Chemistry, Faculty of Sciences, Sakarya University, Sakarya, Türkiye*
[3] *Department of Metallurgy, Gümüşova Vocational School, Duzce University, Düzce, Türkiye*
[4] *Department of Physics, Faculty of Arts and Sciences, Duzce University, Düzce, Türkiye*
[5] *Department of Civil Engineering, Faculty of Engineering, Duzce University, Düzce, Türkiye*
[6] *R&D Department, Fibrobeton Inc., Istanbul, Türkiye*

Received: 29 November 2025
Accepted: 13 February 2026

ABSTRACT

This study investigates frequency-dependent dielectric and electrical transport properties of glass fiber-reinforced concrete (GFRC) systematically doped with ZnO-based hybrid composite (ZnO-@) nanoparticles at 1%, 2%, and 3% mass fractions. Electrical impedance spectroscopy (20 Hz–5 MHz) coupled with microstructural characterization (SEM–EDX, FTIR) and mechanical validation establishes concentration-dependent polarization mechanisms governing electromagnetic property modulation. The 2% ZnO-@ formulation exhibits optimal dielectric enhancement with maximum real permittivity (ε′), superior AC conductivity (100 Hz–10 kHz domain), and 100% imaginary modulus augmentation (M″), attributed to Maxwell–Wagner-Sillars interfacial polarization at ZnO-cement matrix boundaries. Equivalent circuit modeling reveals that grain boundary resistance escalates to 5.8 MΩ at optimal doping, and constant phase element (CPE) exponent values ($P = 0.77–0.84$) confirming non-Debye relaxation due to hierarchical microstructural heterogeneity. The critical percolation threshold, between 2% and 3% ZnO concentration, demarcates the transition from capacitive to conductive behavior, where specimens at 3% exhibit dielectric parameter regression toward baseline values due to nanoparticle agglomeration and the formation of conductive pathways. Spectroscopic validation confirms the integration of wurtzite-phase ZnO (Zn–O: 474 cm^{-1}) with preserved calcium silicate hydrate phases, while post-aging Leeb hardness measurements demonstrate 171–176% mechanical reinforcement (387–456 HLD), validating the retention of structural durability. These findings establish quantitative compositional guidelines for engineering multifunctional

Address correspondence to E-mail: dogu.ramazanoglu@gedik.edu.tr

https://doi.org/10.1007/s10854-026-16810-2
Published online: 06 April 2026

construction composites with tailored electromagnetic response characteristics for interference shielding, capacitive energy storage, and electromagnetically compatible innovative infrastructure applications.

1 Introduction

In recent years, the quest for advanced materials with superior dielectric and energy storage properties has gained significant momentum, particularly in the context of concrete applications. New perspectives have been emerging for concrete-related materials and their impact on the environment, and even for energy application [1]. Concurrently, the synthesis and application of nanomaterials in composite systems have become central to the field of materials science research. Investigators are systematically exploring diverse methodologies to incorporate nanomaterials into composite matrices to enhance their functional properties and structural performance. Within the construction sector, nanomaterial integration strategies are being developed to enhance the mechanical, chemical, and physical properties of these materials, making them suitable for innovative building technologies and specialized electrical applications [2–4]. Dielectric materials are essential for various applications, including capacitors and energy storage devices, due to their ability to store electrical energy efficiently. Several factors, including the choice of filler, matrix material, and the overall composite structure, influence the performance of dielectric materials. Several studies have comprehensively investigated the integration of various additives into GFRC and evaluated its dielectric properties, providing a promising spectrum of applications [5, 6]. Yet, such an additive can yield cleaner, safer urban environments [7]. On the other hand, many researchers have focused on ZnO NPs due to their unique optical and chemical properties, which can be easily modified by altering the shape. Because of its versatility in downstream applications, zinc oxide nanoparticles have been the subject of extensive investigation [8]. Zinc oxide nanoparticles are the second most prevalent metal oxide after iron oxide, and they are inexpensive, safe, and easy to manufacture [9]. The physical and chemical properties of zinc oxide nanoparticles can be easily altered by modifying the shape and using other synthesis techniques, precursors, or materials to form the nanomaterial [10]. Zinc oxide nanoparticles, a Group II–VI semiconductor inorganic compound, are commonly used in analytical sensing applications and typically appear as a white powder, insoluble in water. With an energy band gap of 3.37 eV, zinc oxide nanoparticles exhibit remarkable chemical, electrical, and thermal stability [11].

ZnO can be utilized as a photoanode in DSSCs because it is in the minimal conduction band, whereas the maximum valence band is more energetic. The hexagonal wurtzite structure of ZnO allows for effective electron transport. It also facilitates the formation of densely packed ZnO nanostructures [12, 13]. Hydrothermal synthesis is an efficient method for creating ZnO nanostructures with precise form and size. Several factors influence the end product, including reaction duration, temperature, and the composition of the precursor. The technique commonly uses zinc salts and alkaline solutions, with the inclusion of surfactants or solvents influencing the final structures. Reaction temperatures ranging from 120 to 200 °C have been explored, with 150 °C frequently producing homogeneous morphology. The nature of the original seeds, such as $Zn(OH)_2$ or ZnO_2, has a considerable impact on the final form, size, and surface properties of ZnO [14, 15]. Recent advancements have shown that doping ZnO with various elements can significantly enhance its dielectric properties. For instance, studies have demonstrated that doping with rare-earth metals or transition metals can lead to improved dielectric constants and reduced energy losses, making these composites suitable for high-performance applications [16, 17]. The enhancement mechanisms in such systems typically involve: (i) increased interfacial polarization arising from charge accumulation at heterogeneous phase boundaries between semiconducting dopants and the host matrix, (ii) modification of oxygen vacancy concentrations that serve as electron trapping centers, and (iii) formation of secondary interfacial phases with distinct dielectric relaxation characteristics [18]. These interfacial polarization phenomena, governed by Maxwell–Wagner-Sillars theory, become particularly pronounced when the characteristic relaxation time of the system falls within the measurement frequency range, enabling substantial energy storage capacity through space charge accumulation [19].

The unique properties of ZnO, such as its wide bandgap and high thermal stability, make it an attractive candidate for use in composite materials. Doping ZnO not only modifies its electrical characteristics but also affects its structural and optical properties. For example, Gd-doped ZnO has shown promising results in enhancing both dielectric constants and energy density [20, 21]. The incorporation of such doped ZnO into GFRC can potentially lead to a new class of building materials that not only provide structural support but also contribute to energy efficiency through improved dielectric performance. Moreover, the integration of two-dimensional (2D) fillers alongside doped ZnO has been shown to further enhance dielectric properties by increasing interfacial polarization effects and reducing leakage currents [16, 22]. This approach aligns with current trends in material science, where hybrid composites are engineered to achieve a balance between mechanical strength and electrical performance. Meanwhile, Glass Fiber-Reinforced Concrete (GFRC) has gained significant traction in the construction industry due to its unique properties and versatility. Comprising a cementitious matrix reinforced with alkali-resistant glass fibers, GFRC offers a lightweight yet robust alternative to traditional concrete. Its key advantages include enhanced tensile strength, durability, and design flexibility, making it suitable for a wide range of applications, from architectural facades to precast components. The GFRC can be molded into various shapes and finishes, allowing architects to achieve intricate designs while maintaining structural integrity [23, 24]. One of the most notable characteristics of GFRC is its impressive strength-to-weight ratio. Additionally, GFRC's lightweight nature simplifies handling and installation, reducing labor costs and overall project timelines [25]. However, GFRC does have limitations. Its higher initial cost compared to traditional concrete can be a barrier for some projects. Furthermore, while GFRC excels in non-structural applications, it may not be suitable for heavy-duty structural components that require high compressive strength. Additionally, GFRC is susceptible to chemical degradation in harsh environments, necessitating the use of protective coatings to enhance its longevity [26, 27]. While GFRC presents several advantages that make it an attractive option for modern construction, understanding its limitations is essential for optimizing its application in various contexts. The incorporation of composite-doped zinc oxide (ZnO) into glass fiber-reinforced concrete (GFRC) presents a promising avenue for enhancing the performance of construction materials. This study aims to explore the novel dielectric and energy storage behavior of composite-doped ZnO within GFRC composite, addressing the critical need for materials that can withstand high electrical fields while maintaining structural integrity. In conclusion, the exploration of composite-doped ZnO within GFRC composite holds significant promise for advancing the field of construction materials. By leveraging the unique properties of doped ZnO and optimizing composite structures, this research aims to contribute valuable insights into developing high-performance materials that meet the growing demands for energy-efficient and durable construction solutions. The findings from this study will pave the way for future research into innovative applications of dielectric materials in various engineering fields.

2 Materials and methods

2.1 Materials

The GFRC composite mix was designed with a composition comprising 50% silica sand (particle size range 30–35 AFS, 0–1 mm), 45% white Portland limestone cement conforming to TS EN 197-1 standards, and 5% calcined kaolin as a mineral additive. The mix also included a superplasticizer at 0.5% of the cement weight to improve workability, as well as a polymer additive at 5% of the cement weight to enhance performance. The water-to-cement ratio was maintained at 0.35 to ensure optimal hydration. To further strengthen the composite, alkali-resistant glass fibers were added at 3% of the total weight. The GFRC samples were prepared with varying concentrations of ZnO-@ nanoparticles (0%, 1%, 2%, and 3% by weight of the total matrix). The mixture was thoroughly homogenized using a mechanical mixer to ensure uniformity, then cast into molds and cured in a humidity-controlled environment for 28 days.

2.2 Methods

2.2.1 Sample preparation

The white Portland limestone cement used was of type CEM II 42.5R. The dry components, silica sand,

cement, and calcined kaolin, were first blended in a mechanical mixer until a uniform dry mix was obtained. The superplasticizer and polymer additive were then dissolved in the mixing water and gradually introduced into the dry blend. The ZnO-@ nanoparticles were pre-dispersed in a portion of the mixing water using ultrasonication to prevent agglomeration before being added to the mix. The alkali-resistant glass fibers were incorporated last to minimize fiber damage during mixing. The fresh mixture was cast into standard molds, compacted to remove entrapped air, and subsequently cured in a humidity-controlled environment at approximately 95% relative humidity and 23 ± 2 °C for 28 days prior to testing.

2.2.2 The measurement of dielectrical properties

We evaluated the dielectric properties of ZnO-@ doped GFRC composites using a Keithley 2400 SMU and GW Instek 8105G LCR meter connected to a computer via IEEE 488 interface. Parallel-plate electrode configuration was employed to ensure ohmic contact. Measurements were conducted across a frequency range of 20 Hz to 5 MHz at ambient temperature (25 ± 2 °C) and relative humidity of 45 ± 5% all conducted in triplicate. Specifically, adhesive copper conductive labels (copper-backed conductive tape) were affixed to the two opposing flat faces of each specimen, each label measuring 13 mm in length. The sample diameter was 13 mm with a thickness of 7 mm. The adhesive backing ensured close electrical contact between the electrode and the sample surface. During testing, the electrodes were held in firm contact by the parallel-plate fixture, which provided reproducible contact pressure and minimized contact resistance, without requiring additional external shielding or guard-ring electrodes.

Various electrical parameters were analyzed, such as capacitance, dielectric constants (both real and imaginary components), dielectric loss (ε″), Cole–Cole diagram analysis, dissipation factor (tan δ) at both time and frequency, electrical modulus (M′), and impedance characteristics. This extensive analysis facilitated a detailed characterization of the dielectric and electrical behavior of ZnO-@ doped GFRC composite samples under different conditions and frequencies.

2.2.3 Characterization

Additional experimental assessments included CIE Lab* color space analysis using a PCE-CSM 10 spectrophotometer with D65 illuminant and 10° standard observer, and particle size distribution of ZnO-@ determined via laser diffraction using a Malvern Mastersizer 3000 with Hydro EV wet dispersion unit. The microstructure of the samples was investigated using scanning electron microscopy (SEM) and energy-dispersive X-ray spectroscopy (EDX) with an FEI Quanta FEG 250. Specimens were mounted on aluminum stubs using double-sided carbon tape and sputter-coated with a 10 nm gold/palladium layer to ensure adequate surface conductivity. Scanning electron microscopy analyses were performed at an accelerating voltage of 20 kV, yielding high-resolution images of surface morphology and internal microstructural features. This imaging protocol enabled the precise characterization of microstructural attributes, thereby enhancing the understanding of material behavior at the microscale level. The Surface roughness measurements were performed with a Mahr MarSurf PS 10 Mobile Roughness Measuring Device. Hardness tests, conducted in accordance with ISO/IEC 17025 standards, utilized the Equotip Bambino 2/Piccolo 2 device from Proceq, Switzerland. FT-IR spectra were acquired using a SHIMADZU Prestige-21 (200 VCE) spectrometer device with an ATR attachment.

3 Results and discussion

3.1 Morphological and elemental characterization of the hybrid nanofiller

The structural morphology and elemental composition of the synthesized ZnO-based hybrid nanocomposite were examined to evaluate its dual functionality as both a reinforcing filler and an electrical modifier for Glass Fiber-Reinforced Concrete (GFRC).

3.1.1 Morphological characteristics

The SEM micrographs in Fig. 1a and b reveal the hierarchical nature of the hybrid structure. Figure 1a displays the smooth, laminar features of the organic substrate, whereas Fig. 1b highlights the rougher,

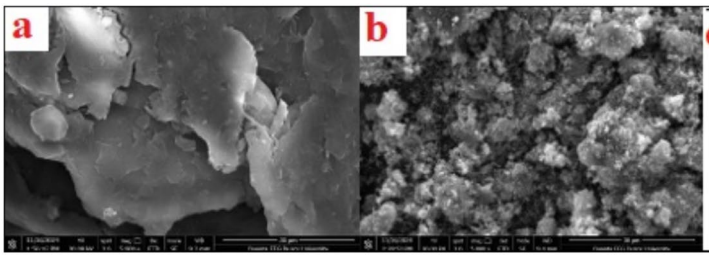

c

Element	Weight %	Atomic %
C	10.8	19.9
N	5.0	7.9
O	41.5	57.6
Zn	42.7	14.5

Fig. 1 SEM micrographs and elemental analysis of the synthesized hybrid nanocomposite: **a** The laminar morphology of the organic matrix, **b** Surface functionalization showing granular ZnO agglomerates, and **c** EDX data quantifying the elemental composition (C, N, O, Zn)

granular surface texture attributed to the deposition of zinc oxide nanoparticles. This distinctive surface roughness is of critical importance for a concrete additive; it serves to enhance the specific surface area available for interaction, thereby promoting mechanical interlocking with the cementitious host matrix and improving the physical integration of the filler.

3.1.2 Elemental composition and dielectric implications

The chemical composition, verified by the EDX analysis presented in Fig. 1c, confirms the successful synthesis of the hybrid system. The dominant concentrations of Zinc (42.7 wt%) and Oxygen (41.5 wt%) validate the presence of the semiconductive ZnO core, which is the fundamental component required for the electrical and dielectric tailoring of the composite.

3.1.3 Significance for GFRC application

Furthermore, the detection of Carbon (10.8 wt%) and Nitrogen (5.0 wt%) is significant. In the context of this study, these elements are not impurities but evidence of effective surface functionalization. This hybrid surface chemistry plays a vital role in the application: the organic groups (indicated by C and N) reduce the surface energy mismatch between the inorganic nanoparticles and the matrix. This mechanism prevents the excessive agglomeration of ZnO during the mixing process, ensuring a homogeneous dispersion throughout the GFRC paste. Consequently, this uniform distribution facilitates the formation of a consistent dielectric network, enabling the effective tailoring of the concrete's electrical properties.

3.2 Particle size analysis of ZnO-@

The resulting particle size distribution graph and associated data are summarized in Table 1. The particle size analysis of the ZnO-@ demonstrates several critical attributes relevant to potential applications. The additive concentration is notably low at 0.0032%, suggesting minimal yet potentially effective incorporation into the composite matrix. The span of the particle size distribution is 5.367, indicating a relatively broad distribution of particle sizes, which is further corroborated by the uniformity value of 1.458, reflecting a moderate level of particle size consistency. The specific surface area is remarkably high at 407.9 m^2/kg, which is advantageous for applications necessitating high surface reactivity. The surface area mean diameter (D [3;2]) is 14.7 µm, while the volume mean diameter (D [4;3]) is 68.3 µm, highlighting the presence of larger particles within the distribution. Additionally, the Dv(10), Dv(50), and Dv(90) values, representing the particle diameters at 10%, 50%, and 90% of the cumulative volume, are 5.40 µm, 36.0 µm, and 199 µm, respectively, indicating a wide range of particle sizes with a significant proportion of larger particles.

Table 1 Results of particle size analysis

Property	Values
Concentration	0.0032%
Span (Particle Size Distribution)	5.367
Uniformity	1.458
Specific surface area	407.9 m^2/kg
D [3;2]	14.7 µm
D [4;3]	68.3 µm
Dv(10)	5.40 µm
Dv(50)	36.0 µm
Dv(90)	199 µm

3.3 FTIR analysis

Fourier transform infrared spectroscopy was systematically employed to elucidate the chemical bonding environment, functional group interactions, and phase composition of ZnO-doped glass fiber-reinforced concrete composites across varying nanoparticle concentrations (1%, 2%, and 3% ZnO-doped), as presented in Fig. 2. The vibrational spectroscopic signatures elucidate nanoparticle-matrix interfacial chemistry, secondary phase formation, and dopant-related effects on dielectric properties.

The broad absorption band observed at $\nu = 3463$ cm^{-1}, with concentration-dependent variations at 3432 cm^{-1} and 3436 cm^{-1}, is characteristic of O–H stretching vibrations. These vibrations arise from surface-adsorbed water molecules and hydroxyl functionalities inherent to cement hydration products, particularly portlandite ($Ca(OH)_2$) and calcium silicate hydrate gel phases [28, 29]. Intensity modulation and slight frequency shifts of this band with progressive ZnO incorporation indicate altered surface chemistry and competitive adsorption dynamics between zinc oxide nanoparticles and moisture at cementitious matrix interfaces [30]. This observation aligns with the established understanding of the hygroscopic nature of ZnO nanostructures, where surface hydroxyl groups play a pivotal role in nanoparticle dispersion stability and interfacial bonding mechanisms [31, 32].

The presence of these hydroxyl signatures in the 3200–3600 cm^{-1} region represents intrinsic characteristics of hydrated cement systems rather than organic contamination, reflecting the fundamental hydration chemistry of calcium silicate phases that constitute the primary binding matrix in concrete formulations [33, 34].Weak but discernible absorption features at $\nu = 2915$ cm^{-1} and $\nu = 3026$ cm^{-1} correspond to aliphatic C–H stretching vibrations (sp^3 hybridization) and aromatic C–H stretching modes (sp^2 hybridization), respectively [35]. These spectral signatures originate predominantly from residual organic coupling agents used in commercial glass fiber surface treatments, typically silane-based sizing compounds such as γ-aminopropyltriethoxysilane or γ-methacryl oxypropyltrimethoxysilane, which are applied during fiber manufacturing to enhance fiber-matrix adhesion and moisture resistance [36]. The persistence of these vibrational modes across all sample compositions confirms the preservation of fiber surface functionality. It validates the structural integrity of the fiber-matrix interfacial region, which is essential for effective stress transfer and mechanical reinforcement in GFRC composites [37]. The relatively high transmittance values (> 95%) associated with these peaks indicate minimal organic contamination and corroborate the predominantly inorganic composition of the composite system [38].The most prominent and diagnostically significant absorption band appears at $\nu = 1036$ cm^{-1}, with shoulder features near 1033 cm^{-1}, corresponding to the asymmetric Si–O–Si stretching vibration (ν_3 mode) within tetrahedral silicate frameworks present in both E-glass fibers (composed primarily of SiO_2–Al_2O_3–CaO–MgO) and calcium silicate hydrate phases formed during cement hydration [39, 40]. This characteristic vibrational mode is well-documented in silicate-based materials, typically manifesting in the 900–1100 cm^{-1} spectral region, and confirms the preservation of the three-dimensional siloxane network throughout composite fabrication and curing processes [41, 42]. The systematic broadening and subtle blue shift of this absorption feature with increasing ZnO-@ concentration suggest enhanced interfacial interactions and potential formation of Zn–O–Si bridging bonds, wherein zinc cations may occupy interstitial or substitutional sites within the silicate structure [43, 44]. This phenomenon has been reported in pozzolanic reaction studies where metal oxide nanoparticles interact with amorphous silica phases to form secondary silicate compounds such as zinc silicate (Zn_2SiO_4, willemite), particularly under alkaline conditions characteristic of cementitious environments

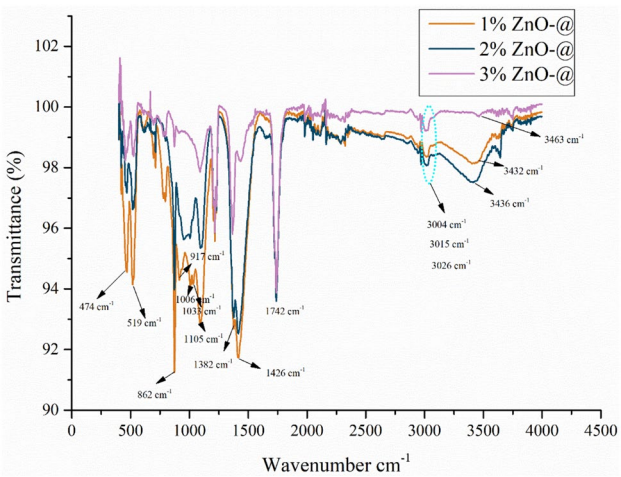

Fig. 2 The obtained FTIR spectrum of ZnO-@ doped GFRC specimens

[45]. The far-infrared region below 700 cm^{-1} contains the most critical spectroscopic evidence for ZnO nanoparticle incorporation and phase identification. The distinct absorption band at $\nu = 474$ cm^{-1} is unambiguously assigned to the characteristic Zn–O stretching vibration corresponding to the E_1 transverse optical phonon mode of wurtzite-phase zinc oxide [46, 47]. This assignment is corroborated by extensive literature on ZnO nanoparticles synthesized via various routes, where the fundamental Zn–O vibrational mode consistently appears in the 400–500 cm^{-1} range, with precise frequency depending on crystallite size, morphology, and defect concentration [48]. The progressive intensification of this band with increasing ZnO-@ loading from 1 to 3% provides quantitative confirmation of the successful integration of nanoparticles and validates the gravimetric formulation of the composite samples [49]. Comparative analysis with reference spectra of pristine ZnO nanopowders demonstrates excellent frequency correlation, substantiating that the incorporated zinc oxide maintains its characteristic wurtzite crystal structure within the GFRC matrix without phase transformation to alternative polymorphs such as zinc blende or rocksalt structures [50, 51]. However, critical examination of the spectral data reveals an additional absorption feature at $\nu = 519$ cm^{-1}, which warrants detailed investigation as this peak does not correspond to the vibrational modes of stoichiometric wurtzite ZnO. Based on comprehensive vibrational spectroscopic databases, this absorption band is tentatively attributed to Cu–O stretching vibrations associated with copper oxide phases, most likely monoclinic cupric oxide (CuO, tenorite structure) [52]. Copper oxide signatures in nominally ZnO-doped materials can arise through several mechanisms: (i) trace transition metal impurities in industrial-grade zinc oxide precursors (typically 0.001–0.1 wt% Cu from zinc ore processing) [53], (ii) contamination during mechanical processing from copper alloy grinding media or reactor vessels, or (iii) deliberate engineering of hybrid core–shell nanostructures wherein excess copper beyond the solubility limit in the wurtzite lattice precipitates as discrete CuO nanophases [54]. The progressive emergence and intensification of this shoulder feature with increasing ZnO-@ content provides compelling evidence that copper originates from the nanoparticle precursor material rather than contamination during composite fabrication. The identified copper oxide phase may contribute to the observed dielectric behavior through charge carrier trapping at Cu-related defect states, modification of oxygen vacancy concentrations, and alteration of grain boundary potential barriers [55, 56]. Bulk CuO exhibits paramagnetic behavior at room temperature (electron configuration Cu^{2+}: $3d^9$, spin $S = 1/2$); the incorporation of paramagnetic centers into the dielectric composite may influence the interfacial polarization mechanisms observed in impedance spectroscopy [57]. However, definitive assessment of copper's contribution requires complementary advanced characterization techniques. X-ray photoelectron spectroscopy would provide quantitative elemental analysis and oxidation state determination, distinguishing between Cu^+ ($3d^{10}$) in cuprous oxide (Cu_2O) and Cu^{2+} ($3d^9$) in cupric oxide (CuO) based on characteristic binding energy shifts and satellite peak structures in the Cu 2p core-level spectra, also electron paramagnetic resonance spectroscopy would enable detection and quantification of paramagnetic Cu^{2+} centers through analysis of characteristic g-factor values and hyperfine coupling patterns [58, 59]. Transmission electron microscopy coupled with energy-dispersive X-ray spectroscopy would enable nanoscale visualization of copper distribution, revealing whether copper exists as homogeneous substitutional dopants within the wurtzite lattice or as phase-separated CuO nanoclusters at grain boundaries. The absorption bands observed at $\nu = 1426$ cm^{-1} and $\nu = 1382$ cm^{-1} are assigned to the asymmetric C–O stretching vibrations of carbonate ions (CO_3^{2-}) arising from atmospheric carbonation reactions that affect the calcium hydroxide and calcium silicate hydrate phases in the cement matrix [60]. This carbonation process, represented by the reaction $Ca(OH)_2 + CO_2 \rightarrow CaCO_3 + H_2O$, is ubiquitous in cementitious materials exposed to ambient atmospheric conditions and represents a natural aging phenomenon rather than contamination [61]. The formation of secondary calcite phases through carbonation has been extensively characterized in concrete durability studies and does not compromise the structural or functional integrity of GFRC composites under normal service conditions [62]. The relatively weak absorption feature at $\nu = 1742$ cm^{-1}, corresponding to C=O stretching vibrations characteristic of carbonyl-containing organic compounds such as esters or ketones, likely originates from residual plasticizers, dispersing agents, or oxidative degradation products of fiber sizing agents [63]. The minimal intensity of this peak, with transmittance changes less than 2%, confirms negligible organic content and validates the

predominantly inorganic composition of the composite system. Systematic comparison of FTIR spectra across the concentration series (1%, 2%, and 3% ZnO-@) reveals several concentration-dependent spectroscopic trends that provide insight into nanoparticle-matrix interactions and dispersion characteristics. The progressive intensification of the Zn–O stretching band at 474 cm^{-1} with increasing ZnO-@ loading demonstrates a direct correlation between nanoparticle concentration and spectroscopic signature intensity, consistent with Beer-Lambert law principles for infrared absorption spectroscopy. The subtle blue shift observed in the Si–O–Si stretching frequency, from approximately 1036 cm^{-1} to 1038 cm-1 with increasing ZnO content, suggests a strengthening of siloxane bridging bonds, potentially arising from ZnO-catalyzed silicate polymerization reactions or the formation of Zn–O–Si interfacial bonding at nanoparticle-matrix interfaces. The broadening of the hydroxyl absorption envelope centered at 3463 cm^{-1} correlates with increased surface area and hydroxyl site density associated with higher nanoparticle concentrations, reflecting the high specific surface area characteristic of nanoscale ZnO particles. Most significantly, the progressive emergence and intensification of the shoulder feature at 519 cm^{-1} with increasing ZnO-@ content support the hypothesis that copper impurities scale proportionally with the ZnO-@ feedstock concentration. The spectroscopic findings have significant implications for understanding the multifunctional properties of ZnO-doped GFRC composites and designing optimized formulations for specific applications. The confirmed presence of wurtzite-phase ZnO nanoparticles validates the successful implementation of nanoparticle reinforcement strategies aimed at enhancing mechanical, dielectric, and potentially electromagnetic shielding properties of conventional GFRC materials. The identification of copper oxide phases, while initially considered an impurity, may serendipitously contribute to functional characteristics relevant to emerging applications in electromagnetic interference shielding, sensor technologies, and smart construction materials with tunable electrical properties through defect-mediated charge transport mechanisms. The coexistence of enhanced interfacial polarization effects observed in electric modulus spectroscopy with trace paramagnetic phases creates opportunities for developing materials with coupled dielectric responses suitable for electromagnetically compatible construction applications. In conclusion, comprehensive FTIR spectroscopic analysis confirms successful incorporation of wurtzite-phase ZnO nanoparticles within the GFRC matrix while identifying trace copper oxide phases that may contribute to the composite's dielectric characteristics. The characteristic vibrational modes associated with hydroxyl groups, silicate networks, carbonate phases, and metal oxide frameworks collectively validate the complex chemical composition and interfacial interactions governing the functional properties of these multiphase composites.

3.4 SEM & EDS analysis

SEM and EDS analyses provide comprehensive insight into the microstructural and elemental composition of 1% ZnO-@ doped GFRC specimens. The SEM image reveals distinct microstructural features, including micro gaps, ettringite, ZnO-@ particles, and calcium hydroxide (CH). Notably, the presence of calcium silicate hydrate (C–S–H) is highlighted, which is crucial for concrete's mechanical strength and durability (Fig. 3). The EDS spectrum complements this by identifying the elemental constituents and their respective weight percentages: carbon (9,30%), oxygen (49.4 %), aluminum (2.20%), silicon (7.40%), sulfur (1.50%), potassium (0.20%), calcium (27.5%), copper (2.20%), and zinc (0.40%). This detailed characterization underscores the successful incorporation of ZnO-@ into the GFRC matrix, potentially enhancing the material's mechanical properties and durability. Such analyses are pivotal for advancing the understanding and development of high-performance construction materials.

The SEM and EDS analysis results provide a thorough understanding of the microstructural and elemental makeup of a 2% ZnO-@ doped GFRC composite specimen. The SEM images showcase notable microstructural characteristics, such as micro gaps, ettringite, ZnO-@ particles, and calcium hydroxide (CH). Importantly, the presence of calcium silicate hydrate (C–S–H) is emphasized, as it plays a vital role in the mechanical strength and durability of concrete (Fig. 4).

Complementing this, the EDS spectrum identifies the elemental components along with their respective weight percentages: carbon (6,60%), oxygen (55,8%), magnesium (0,40%), aluminum (2,40%), silicon (6,20%), sulfur (1,70%), calcium (24,3%), copper (2,30%), and zinc (0,30%). This comprehensive characterization highlights the effective integration of ZnO-@

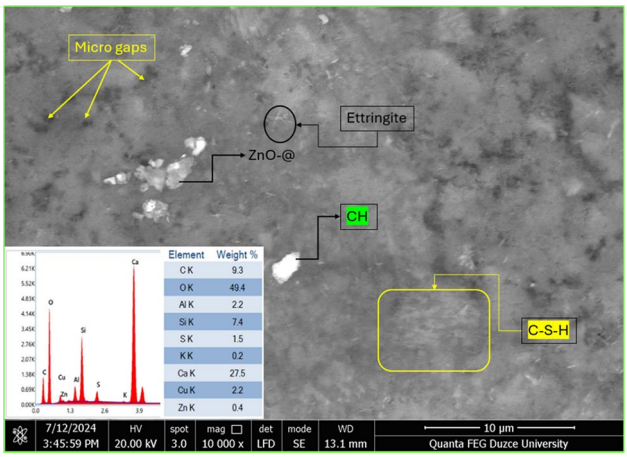

Fig. 3 The SEM image of the GFRC specimen surface doped with 1% ZnO-@

into the GFRC matrix, which may enhance the material's mechanical properties and overall durability.

The incorporation of 3% ZnO into GFRC significantly influences the microstructural and mechanical properties of the composite material (Fig. 5). The SEM micrograph provides a detailed visualization of the microstructural features, which are crucial for assessing the material's performance. The presence of ettringite and C–S–H phases indicates the ongoing hydration reactions and the formation of binding phases that contribute to the material's strength and durability. Based on the Energy-dispersive X-ray spectroscopy (EDX) analysis, the ZnO-doped Glass Reinforced Concrete (GFRC) sample contains approximately 4,20% carbon, 50,6% oxygen, 1,70% aluminum, 6,90% silicon, 1,00% sulfur, 26,5% calcium, 8,80% copper, and 0,50% zinc. These elemental percentages provide a comprehensive understanding of the sample's composition, which is crucial for evaluating its properties and potential applications. The high oxygen content indicates the presence of various oxides, while the significant amounts of silicon and calcium suggest the formation of calcium silicate hydrate (C–S–H) phases, contributing to the material's strength. The zinc doping, confirmed by the 0.50% zinc content, is expected to enhance the photocatalytic and antimicrobial properties of the concrete, making it suitable for advanced construction applications.

Furthermore, the micro gaps observed in the SEM image may indicate potential areas for improvement in the mixing and curing processes to achieve a more homogeneous distribution of ZnO particles. Addressing these microstructural inconsistencies could lead to enhanced mechanical properties and longevity of the GFRC.

In conclusion, the 3% ZnO-doped GFRC sample demonstrates promising characteristics for advanced construction applications. Future research should focus on optimizing the doping process and investigating the long-term performance of ZnO-doped GFRC under various environmental conditions.

3.5 Surface roughness analysis

Table 2 presents the surface roughness parameters of ZnO-@ before and after the aging process. The parameters measured include Ra (average roughness), Rz

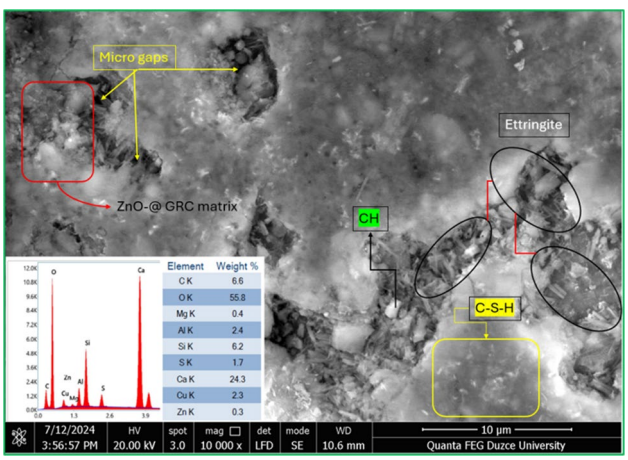

Fig. 4 The SEM image of the GFRC specimen surface doped with 2% ZnO-@

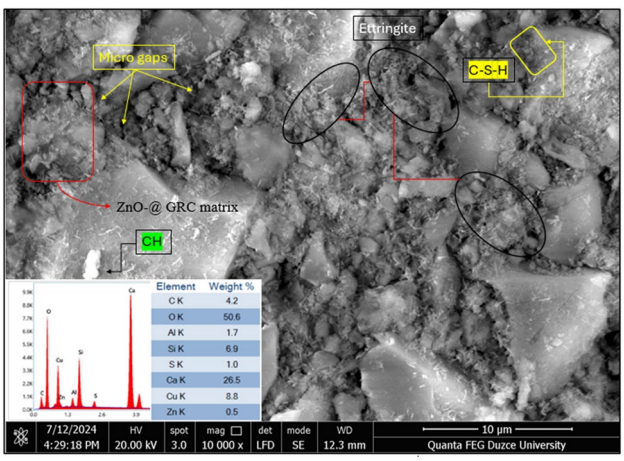

Fig. 5 The SEM image of the GFRC specimen surface doped with 3% ZnO-@

(mean peak-to-valley height), and Rmax (maximum roughness depth). Before aging, the Ra values for ZnO-@ at concentrations of 1%, 2%, and 3% were 0.13, 0.59, and 0.94, respectively (Table 2). After aging, these values changed to 0.39, 0.36, and 1.07, indicating increases of 200%, − 38.98%, and 13.83%, respectively. For Rz, the initial values were 2.05, 7.09, and 8.86, which changed to 3.34, 3.64, and 9.66 after aging, reflecting changes of 62.93%, − 48.66%, and 9.02%. The Rmax values initially recorded were 2.23, 17.1, and 10.0, which shifted to 1.95, 1.80, and 5.35 after aging, indicating variations of − 12.56%, − 89.47%, and − 46.5%. These results highlight significant changes in surface roughness parameters due to the aging process, with some parameters increasing and others decreasing, indicating complex interactions affecting the ZnO-@ surface morphology.

3.6 Color analysis of ZnO-@ doped GFRC samples

Table 3 presents color parameters of ZnO-@-doped GFRC specimens before and after the aging process, focusing on the L* (lightness), a* (red–green), and b* (yellow–blue) values. Initially, the L* values for ZnO-@ at concentrations of 1%, 2%, and 3% were 44.9, 43.7, and 41.1, respectively. After aging, these values changed to 46.3, 38.9, and 28.9, indicating percentage changes of 3.12%, − 10.98%, and − 29.68%, respectively. The color parameter a* values initially were 2.11, 2.13, and 2.80, which altered to 2.00, 2.07, and 1.80 post-aging, reflecting changes of − 5.21%, − 2.82%, and − 35.71%. For the b* values, the initial readings were 3.29, 2.49, and 4.31, which shifted to 2.78, 2.70, and 2.51 after aging, indicating variations of − 15.50%, 8.43%, and − 41.76%. These results demonstrate that the aging process significantly affects the color parameters of ZnO-doped GFRC composite specimens, with notable increases and decreases in lightness and chromaticity values, indicating complex interactions that influence the material's appearance.

3.7 Leeb hardness measurements of ZnO-@ doped GFRC specimens

Table 4 presents the Leeb hardness measurements of ZnO-doped GFRC composite before and after the aging process. Initially, the hardness values for the 1%, 2%, and 3% ZnO-@ composites were 165, 154, and 143 HLD, respectively. After aging, these values significantly increased to 456, 417, and 387 HLD, respectively. This represents an increase of approximately 176%, 171%, and 171% for the 1%, 2%, and 3% composites, respectively.

The substantial increase in hardness after aging can be attributed to incorporating ZnO nanoparticles, which enhance the mechanical properties of the concrete matrix. The other components of the ZnO-@ likely contribute to this improvement. These components act as reinforcing agents, improving the dispersion of ZnO nanoparticles and preventing their accumulation, which enhances the overall matrix structure. Additionally, they may contribute to the formation of a more robust and interconnected network within the cement matrix, further enhancing its mechanical properties. These doped materials interact synergistically with the cement matrix, significantly improving hardness after the aging process.

3.8 Dielectric properties

To elucidate the electrical behavior, we measured capacitance (C) and conductance (G) of ZnO-doped GFRC composites. The dielectric parameters were

Table 2 Surface roughness before (*) and after (**) aging

Sample	Parameter	1%	2%	3%
ZnO-@ (*)	Ra	0.13	0.59	0.94
	Rz	2.05	7.09	8.86
	Rmax	2.23	17.1	10.0
ZnO-@ (**)	Ra	0.39	0.36	1.07
	Rz	3.34	3.64	9.66
	Rmax	1.95	1.80	5.35

(*) Before aging, (**) After aging

Table 3 Color analysis before (*) and after (**) aging

Sample	Content (%)	L*	a*	b*
ZNO-@ (*)	1	44.9	2.11	3.29
	2	43.7	2.13	2.49
	3	41.1	2.80	4.31
ZNO-@ (**)	1	46.3	2.00	2.78
	2	38.9	2.07	2.70
	3	28.9	1.80	2.51

(*) Before aging, (**) After aging

Table 4 Leeb hardness measurement before (*) and after (**) aging

Sample	Content (%)	HLD
ZnO-@ (*)	1	165
	2	154
	3	143
ZnO-@ (**)	1	456
	2	417
	3	387

(*) Before aging, (**) After aging

calculated from the C and G readings using the proper formalism as below. All data were obtained from the measurement system by Keithley 2400 SMU and GW Instek 8105 LCR meter using the following equations [1, 64, 65]:

$$C_0 = \varepsilon_0 \frac{A}{d} \quad (1)$$

$$\varepsilon^* = \varepsilon' + j\varepsilon'' \quad (2)$$

$$\varepsilon' = \frac{C}{C_0} \quad (3)$$

$$\varepsilon'' = \frac{G}{\omega C_0} \quad (4)$$

$$tan\delta = \frac{\varepsilon''}{\varepsilon'} \quad (5)$$

The complex real permittivity ε* as a function of angular frequency is made up of ε′, the real part related to energy storage, and ε″, the imaginary part representing dielectric loss. Here, $\varepsilon_0 = 8.85 \times 10^{-14}$ F·cm^{-1} represents the permittivity of free space, C_0 denotes the capacitance of the empty measurement cell (geometric capacitance without sample), tan δ is the loss tangent (dissipation factor), and ω is the angular frequency.

A represents the active contact area, while d represents the thickness of the sample examined. The capacitance-frequency (*C*–f) characteristics of ZnO-doped glass-reinforced concrete (GFRC) samples compared to the undoped reference are presented in Fig. 6a. All studied samples exhibited a decrease in capacitance with increasing frequency, ranging from 100 Hz to 1 MHz, indicating dispersive behavior typical

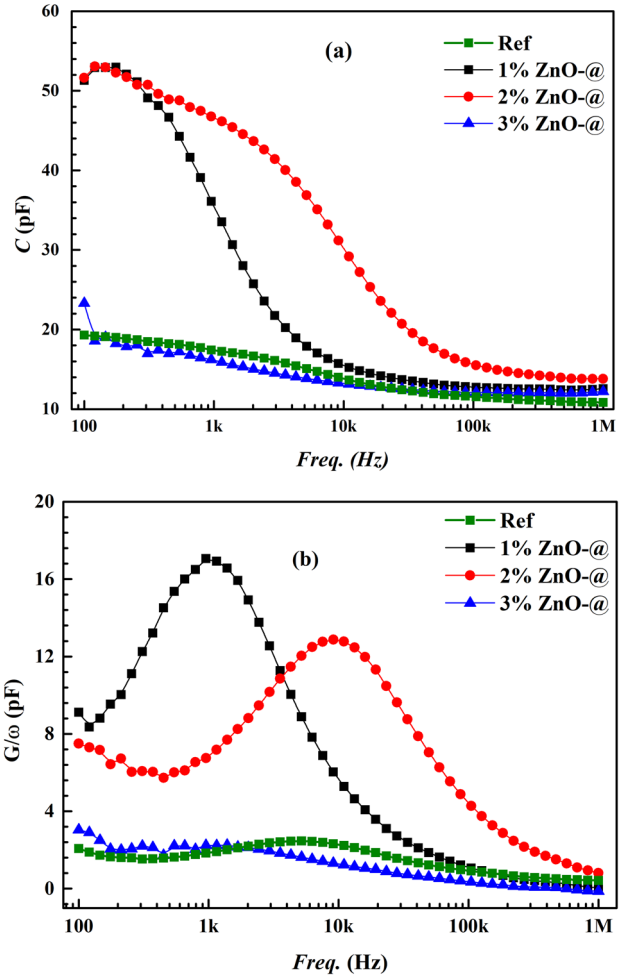

Fig. 6 **a** The Capacitance (*C-f*) and **b** normalized conductance (*G/ω*), which is proportional to the imaginary permittivity (ε″) characteristics of ZnO-doped GFRC composite

of cementitious materials, while the addition of ZnO particles significantly alters the dielectric response of GFRC samples, particularly at lower frequencies (100 Hz–10 kHz). Regarding the concentration-dependent behavior, 1% ZnO particle doping yielded a moderate increase in capacitance values compared to the reference. The 2% ZnO doping shows the most pronounced effect, with the highest capacitance values across most of the frequency range. Surprisingly, 3% ZnO doping leads to capacitance values closer to those of the reference sample, suggesting a possible saturation effect. On the other hand, the impact of ZnO doping on Low-frequency enhancement is most evident below 10 kHz, where the doped samples (especially 2% ZnO) exhibit substantially higher capacitance than the reference sample. Meanwhile, above 100 kHz, the

capacitance values of all samples converge, indicating that ZnO doping primarily affects low-frequency dielectric behavior. Upon the addition of ZnO composite, a non-linear doping response was realized in the obtained results. Clearly, the non-monotonic change in capacitance with increasing ZnO concentration (2% > 1% > 3%) refer to complex interactions between the dopant and the GFRC composite matrix which necessitates further evaluation frequency-dependent normalized conductance (G/ω) characteristics of the samples, which directly relate to the imaginary part of the complex permittivity ($\varepsilon'' \propto G/\omega$), can be seen from Fig. 6b. The examined measurements span from 100 Hz to 1 MHz, providing insight into the GFRC's response across a wide frequency spectrum. The undoped reference sample exhibited relatively low and stable conductance values across the frequency range. While the ZnO composite doping significantly alters the conductance behavior, with the effect varying by concentration. The conductance characteristics of ZnO-doped GFRC samples exhibit distinct patterns across varying concentrations of doping. The 1% ZnO-doped sample demonstrates the most pronounced conductance peak, centered around 1 kHz. In contrast, the 2% ZnO-doped sample displays a notable but reduced peak, shifted towards higher frequencies (approximately 10 kHz). Interestingly, the 3% ZnO-doped sample shows conductance values more closely aligned with the undoped reference, suggesting a potential saturation point or alteration in conduction mechanisms at elevated doping levels. Both 1% and 2% ZnO-doped samples exhibit well-defined, bell-shaped conductance profiles, indicative of relaxation processes. These processes may be attributed to interfacial polarization or charge carrier hopping mechanisms. In the low-frequency range (< 1 kHz), the 1% ZnO-doped sample outperforms the 2% sample in terms of conductance. However, this trend inverts at higher frequencies, with the 2% sample maintaining superior conductance beyond the peak frequencies. As frequencies approach 1 MHz, all samples converge towards similar, low conductance values. This convergence implies that ZnO doping exerts its most significant impact on conductance within the low to mid-frequency range. These findings suggest that ZnO doping can be effectively employed to modulate the dielectric properties of GFRC, with potential applications in enhancing electrical response or energy storage capabilities. The optimal doping concentration appears to be approximately 2% ZnO, beyond which further doping may yield diminishing returns or even adversely affect the material's capacitive behavior. The observed conductance peaks and their frequency shifts relative to doping concentration provide valuable insights into the charge transport mechanisms within the composite. The optimal doping level is contingent upon the desired operational frequency range, with 1% and 2% ZnO exhibiting enhanced conductance across different frequency bands. The unexpected behavior of the 3% ZnO-doped sample warrants further investigation, for the frequency dependence of the real and the imaginary permittivity ($\varepsilon'$and ε'') for ZnO-doped composite samples with varying concentrations (1%, 2%, and 3%) compared to an undoped reference sample were evaluated by employing Eqs. (3) and (4), respectively.

The real part ε' of permittivity was obtained across a frequency range of 100 Hz to 1 MHz. it was observed that all samples exhibit a decrease in ε' with increasing frequency, indicating dielectric relaxation processes typical in composite materials. Also, the doping amount declared that ZnO composite significantly alters the dielectric behavior of GFRC, particularly at lower frequencies. The 1% and 2% ZnO samples show markedly higher ε' values compared to the reference, especially below 10 kHz. Regarding the concentration-dependent response, 1% ZnO doping yielded the highest ε' values at very low frequencies (< 500 Hz), while 2% ZnO doping exhibited the highest ε' values over a broader frequency range (500 Hz–100 kHz). Interestingly, 3% ZnO doping leads to ε' values similar to or slightly below the reference sample. The dielectric behavior of ZnO-doped GFRC samples exhibits distinct characteristics across different frequency ranges and doping concentrations. In the low-frequency domain, particularly below 1 kHz, the 1% and 2% ZnO-doped samples demonstrate a marked increase in real permittivity (ε'), indicative of strong interfacial polarization effects. Notably, the 2% ZnO-doped sample maintains elevated ε' values across a broader frequency spectrum compared to its 1% counterpart. As frequencies exceed 100 kHz, a convergence in ε' values is observed across all samples, suggesting that ZnO doping predominantly influences the low-frequency dielectric response. The 1% and 2% ZnO-doped samples exhibit more pronounced relaxation behavior, evidenced by a steeper decline in ε' as frequency increases. These findings highlight the potential of ZnO doping to significantly enhance the dielectric permittivity of GFRC materials, particularly at lower

frequencies. The optimal doping concentration appears to be approximately 2% ZnO, which sustains elevated ε′ values over the broadest frequency range. The unexpected behavior observed in the 3% ZnO-doped sample suggests a potential saturation effect or structural alterations at higher doping levels, warranting further investigation. The enhanced low-frequency permittivity in doped samples can be attributed to increased interfacial polarization, possibly resulting from the formation of space charge regions at ZnO-concrete interfaces. This property could prove advantageous for applications requiring high dielectric constants at lower frequencies, such as energy storage devices or sensing systems. The convergence of ε′ values at higher frequencies indicates that ZnO doping primarily influences slower polarization mechanisms, while faster electronic and atomic polarizations remain relatively unaffected. This insight provides valuable information for tailoring the dielectric properties of GFRC materials for specific frequency-dependent applications. On the other hand, frequency-dependent behavior of the imaginary part of dielectric permittivity (ε″) for ZnO-doped glass-reinforced concrete (GFRC) samples across a frequency range of 100 Hz to 1 MHz can be seen from Fig. 6b to further insights into dielectric loss mechanisms. It was found that ZnO doping significantly modifies the ε″ behavior, particularly at lower frequencies. The 1% and 2% ZnO-doped samples exhibited pronounced peaks in ε″, indicating strong dielectric loss mechanisms absent in the reference sample. The response is concentration-dependent: 1% ZnO displays the highest ε″ peak, centered around 1–2 kHz, while 2% ZnO shows a lower but broader peak, shifted to higher frequencies (approximately 10 kHz). Interestingly, 3% ZnO unexpectedly exhibits ε″ values close to or below the reference, mirroring its behavior in ε′. The peaks in ε″ for 1% and 2% ZnO samples correspond to the regions of steepest decline in ε′ (Fig. 7a), confirming the presence of dielectric relaxation processes. The shift in peak frequency from 1 to 2% ZnO suggests a change in the dominant relaxation mechanism with increased doping. In the low-frequency domain, unlike ε′, which showed a monotonic increase, ε″ for 1% and 2% ZnO samples display a slight decrease below 1 kHz, indicating a transition between different loss mechanisms. At high frequencies (above 100 kHz), all samples were converged to low ε″ values, consistent with the behavior observed in ε′. The frequency ranges where ε″ peaks occur correspond to the regions of highest dispersion in ε′, indicating that the same physical processes are responsible for both energy storage (ε′) and energy dissipation (ε″) in the material. These results, when combined with the ε′ data, provide a comprehensive picture of the dielectric behavior in ZnO-doped GFRC. The appearance of loss peaks in the 1% and 2% ZnO samples suggests the introduction of new relaxation mechanisms, possibly related to interfacial polarization at the ZnO-GFRC interfaces or charge carrier hopping. The shift in peak frequency between 1 and 2% ZnO indicates that increasing the dopant concentration not only enhances the magnitude of the dielectric response but also alters its frequency dependence. In addition, Fig. 7c shows how the dielectric loss tangent (tanδ) varies with frequency for varied amounts of composite-doped ZnO in GFRC composite. The dissipation factor (Tanδ) is the ratio of energy lost by a material to the total energy in a circuit. The Tanδ was calculated using the Eq. (5). Figure 7 c complements the previous analyses of ε′ and ε″, offering insights into the overall dielectric loss characteristics across a frequency range of 100 Hz to 1 MHz. ZnO doping was found to be significantly modifies the tan δ behavior, particularly in the mid-frequency range. The 1% and 2% ZnO-doped samples exhibited pronounced peaks in tan δ, indicating frequency ranges of maximum dielectric loss. The response is concentration-dependent: 1% ZnO displays the highest tan δ peak, centered around 2–3 kHz, while 2% ZnO shows a lower but broader peak, shifted to higher frequencies (approximately 20–30 kHz). Notably, 3% ZnO unexpectedly exhibits tan δ values similar to or below the reference, consistent with its behavior in ε′ and ε″. The tan δ peaks for 1% and 2% ZnO samples closely correspond to the ε″ peaks observed in Fig. 7b, confirming the frequency ranges of maximum energy dissipation. The shift in peak frequency from 1 to 2% ZnO further supports the change in dominant relaxation mechanisms with increased doping. In the low-frequency domain, all samples show a slight increase in tan δ at very low frequencies (< 200 Hz), suggesting the onset of a different loss mechanism, possibly related to DC conductivity. At high frequencies (above 100 kHz), tan δ values for all samples tend to converge, consistent with the behavior observed in ε′ and ε″ part. Also, it was realized that tan δ peaks occur at frequencies where ε′ shows the steepest decline and ε″ exhibits maxima, providing a comprehensive view of the dielectric relaxation processes. Based on those contributions, it can be said that the appearance of distinct tan

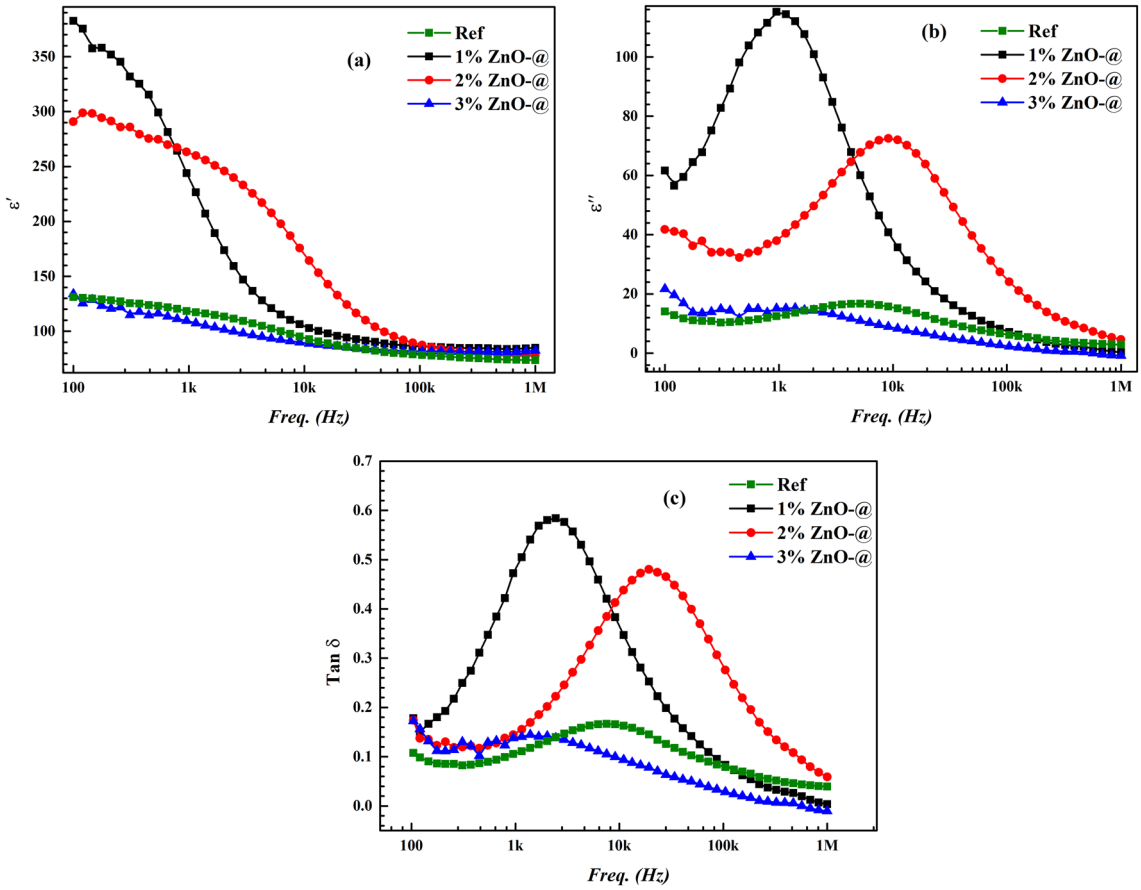

Fig. 7 Frequency-dependent dielectric characteristics of ZnO-doped GFRC composites: **a** real permittivity (ε′), **b** imaginary permittivity (ε″), and **c** loss tangent (tan δ)″

δ peaks in the 1% and 2% ZnO samples confirms the introduction of new energy dissipation mechanisms due to ZnO particles doping to the GFRC sample. Additionally, the shift in peak frequency between 1 and 2% ZnO indicates that increasing dopant concentration affects both the magnitude of dielectric loss and its frequency dependence. The tan δ data corroborate the earlier hypothesis that a 1–2% ZnO doping range represents an optimal range for enhancing dielectric properties. The unexpected behavior of the 3% ZnO sample across all dielectric parameters strongly suggests a critical concentration beyond which additional ZnO becomes ineffective or possibly detrimental to the dielectric properties. In conclusion, the combined analysis of ε′, ε″, and tan δ reveals that ZnO doping can be used to engineer the frequency-dependent dielectric properties of GFRC materials precisely. This tunable behavior, particularly the ability to control the frequency of maximum dielectric loss, could be exploited in applications such as electromagnetic interference shielding or energy storage devices, where specific dielectric loss characteristics are crucial.

Meanwhile, the real part of the electrical modulus (M′) characteristics of ZnO concrete samples, compared with a control sample, were analyzed across different ZnO addition ratios using the corresponding ε′ and ε″ values for the studied ZnO doped GFRC composite. The components were determined using the following equations:

$$M^* = \frac{1}{\varepsilon^*} = M' + jM'' = \frac{\varepsilon'}{\varepsilon'^2 + \varepsilon''^2} + j\frac{\varepsilon''}{\varepsilon' + \varepsilon''^2} \tag{6}$$

The frequency range examined was from 100 Hz to 1 MHz. The results, depicted in Fig. 8a, reveal a sigmoidal trend across all samples, with M′ values increasing from low to high frequencies before plateauing. The control sample (Ref) consistently exhibited the lowest modulus values across the frequency spectrum. In contrast, the ZnO concrete samples

demonstrated progressively higher electrical modulus values with increasing ZnO content. Specifically, the 1% ZnO sample showed a moderate increase in M′ values, while the 2% and 3% ZnO samples exhibited more pronounced increases, indicating a clear enhancement in electrical properties with higher ZnO concentrations. It can be concluded that the incorporation of ZnO into GFRC composite significantly influences its electrical characteristics, with higher ZnO ratios leading to improved electrical modulus values. This enhancement is likely due to the conductive nature of ZnO, which facilitates better charge transport within the concrete matrix. Also, the imaginary part of electrical modulus M″ as a function of frequency for ZnO-doped GFRC samples with varying concentrations (1%, 2%, and 3%) compared to an undoped reference sample was evaluated too and is illustrated in Fig. 8b. The results obtained revealed distinct relaxation peaks for each sample, indicating the presence of different relaxation processes. The reference sample exhibits a broad peak centered around 10 kHz, while the ZnO-doped samples show more pronounced and shifted peaks. The 1% ZnO-doped sample displays the highest M″ peak magnitude, occurring at approximately 5 kHz. The 2% ZnO-doped sample shows a peak of slightly lower magnitude but shifted to a higher frequency of approximately 50 kHz. Interestingly, the 3% ZnO-doped sample exhibits a significantly suppressed peak, with its maximum occurring at the lowest frequency among all samples, around 500 Hz. Our findings suggest that ZnO doping has a significant influence on the dielectric relaxation behavior of GFRC. The shift in peak frequencies and changes in peak magnitudes with varying ZnO concentrations indicate alterations in the charge carrier dynamics and polarization mechanisms within the material. The non-linear relationship between ZnO concentration and peak characteristics implies complex interactions between the dopant and the GFRC matrix, potentially affecting the material's electrical properties and microstructure.

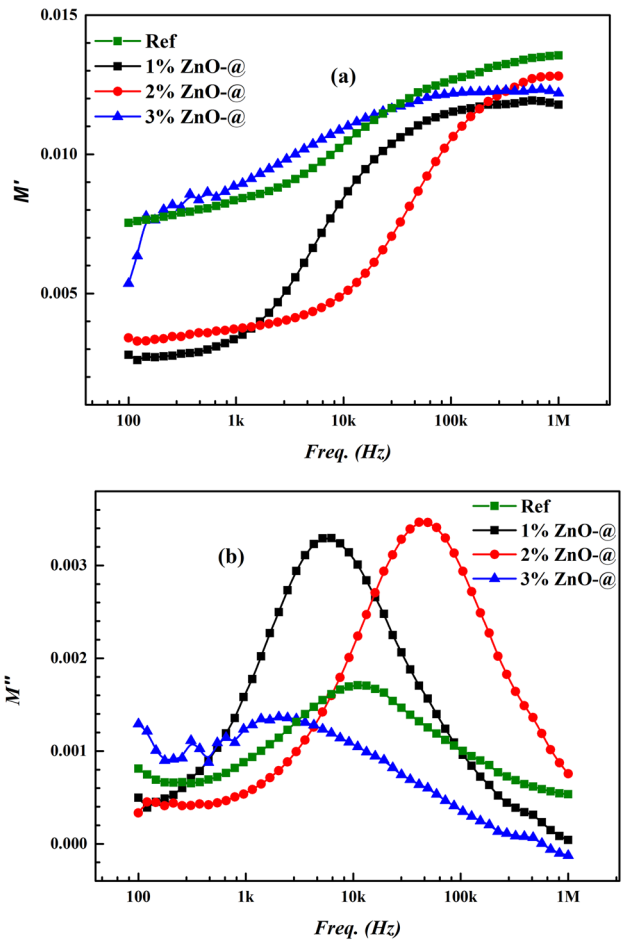

Fig. 8 **a** Real part **b** imaginary part of electrical modulus characteristics of ZnO-@ doped GFRC composite

Further evaluation was obtained as the variation of real permittivity (ε″) with Energy (ε′) for Different Concentrations of ZnO-@ doped GFRC composite namely Cole–Cole plot and illustrated in Fig. 9a. Cole–Cole plots reveal distinct dielectric behavior between the reference sample and ZnO-doped GFRC composites at varying concentrations (1%, 2%, and 3%). The reference sample (Ref) exhibits the largest semicircle, indicating a higher overall dielectric response compared to the ZnO-doped samples. Its curve extends from approximately $\varepsilon' = 50$ to $\varepsilon' = 375$, with a maximum ε″ value reaching about 115. As the ZnO doping concentration increases, a clear trend of decreasing semicircle size is observed. The 1% ZnO sample showed a smaller semicircle compared to the reference, with ε′ ranging from about 50 to 300 and a maximum ε″ of approximately 75. The 2% ZnO sample further reduced in size, with ε′ spanning from about 50 to 250 and a peak ε″ of roughly 70. The 3% ZnO sample displays the smallest semicircle, suggesting the most significant alteration in dielectric properties. Its curve is notably compressed, with ε′ ranging only from about 50 to 150 and a maximum ε″ of approximately 20. This systematic reduction in semicircle size with increasing ZnO concentration indicates that ZnO doping progressively modifies the dielectric relaxation processes within the GFRC composite. The shrinking semicircles suggest a decrease in the overall polarizability of the material, potentially accompanied by faster relaxation times with higher ZnO content. Our

observations suggest that ZnO doping effectively tunes the dielectric properties of GFRC composite, with higher concentrations resulting in more pronounced changes. This tuning capability could be advantageous for tailoring the material's electromagnetic response for specific applications in construction or electronic industries**.** Figure 9b, presents the Argand plot diagrams for glass fiber-reinforced concrete (GFRC) samples doped with varying concentrations of ZnO, compared to a control sample. Argand plots revealed significant changes in the dielectric properties of GFRC with the addition of ZnO. The control sample exhibited the highest peak in the Argand plot, indicating the maximum dielectric loss. As the ZnO concentration increases from 1 to 2% and 3%, a consistent trend of decreasing peak height is observed. This reduction in peak height suggests that ZnO doping effectively lowers the dielectric loss in GFRC samples. Also, a notable shift in peak position towards lower M′ values was evident with increasing ZnO content. This shift can be attributed to alterations in the polarization processes within the GFRC composite matrix due to the presence of ZnO particles. The observed trend implies that ZnO doping modifies the electrical conductivity and polarization characteristics of the GFRC composite. The systematic changes in both peak height and position with increasing ZnO concentration suggest a direct relationship between ZnO content and the dielectric properties of GFRC composite. This relationship can be explained by the interaction between ZnO particles and the cementitious matrix, which likely alters the microstructural pathways for charge transport and polarization. The 3% ZnO-doped sample shows the most pronounced effects, with the lowest peak height and the furthest shift towards lower M′ values. This observation indicates that higher concentrations of ZnO have a more significant impact on reducing dielectric loss and modifying polarization characteristics in GFRC. Our findings suggest that ZnO doping could be an effective method for tuning the dielectric properties of GFRC composites. The ability to reduce dielectric loss through ZnO addition may have important implications for applications requiring enhanced electromagnetic shielding or improved insulative properties in construction materials.

The electric modulus formalism ($M^* = 1/\varepsilon^*$) was employed to investigate the interfacial polarization mechanisms and charge carrier dynamics in ZnO-@ doped GFRC composites, as depicted in the Argand diagram (M″ vs M′, Fig. 9b). This representation effectively suppresses electrode polarization artifacts and emphasizes bulk relaxation processes, providing complementary insights to the conventional Cole–Cole analysis [66, 67]. Based on the results obtained from Fig. 9b, it can be stated that the Argand plots exhibit characteristic semicircular arcs corresponding to non-Debye relaxation processes. The reference sample demonstrated M″ max ≈ 0.0017 centered at M′ ≈ 0.0070, establishing baseline dielectric relaxation governed by cement hydration products and fiber-matrix interfacial polarization. Notably, the Progressive ZnO incorporation yielded a biphasic response: enhancement phase (1–2% ZnO-@) with M″ max increasing to 0.0034 (100% enhancement), followed by degradation phase (3% ZnO-@) with M″ max declining to 0.0014. This non-monotonic behavior indicates a critical percolation threshold between 2 and 3% ZnO concentration, consistent with interfacial polarization theory in heterogeneous dielectric systems [68, 69]. Furthermore, to elucidate the charge transport mechanisms

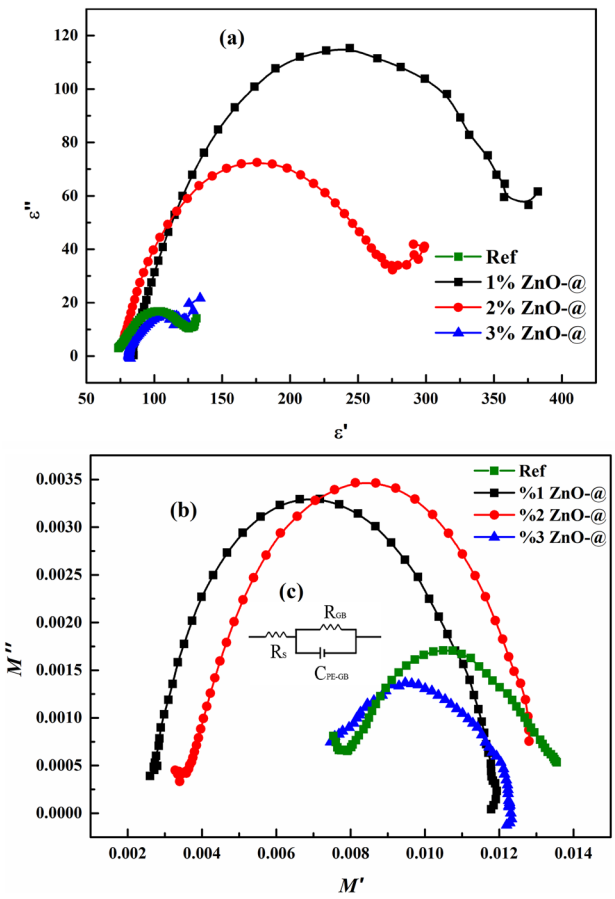

Fig. 9 **a** The Cole–Cole (imaginary vs. real permittivity, ε″ vs. ε′) plot diagrams, and **b** the Argand diagrams of ZnO-@ doped GFRC composite, **c** the obtained equivalent circuit

and interfacial polarization dynamics, the impedance spectroscopy data were systematically fitted to a modified Debye equivalent circuit model comprising series resistance or electrode contact resistance (Rs) in combination with a parallel arrangement of grain boundary resistance (RGB) and constant phase element or non-ideal capacitance (C_{PE}), represented as: Rs + (R_{GB}||C_{PE}) [70–72] which can be seen from Fig. 9c. This circuit topology accurately illustrates the contribution of electrode contact resistance (Rs) and the non-ideal interfacial relaxation behavior governed by grain boundary resistance. The constant phase element, which replaces the ideal capacitor to account for dispersive dielectric relaxation inherent to heterogeneous materials, exhibits impedance described by $Z_{CPE} = 1/[T(j\omega)^P]$, where T represents the C_{PE} coefficient ($F \cdot s^{(P-1)}$), ω denotes angular frequency. The exponent P quantifies deviation from ideal Debye behavior, with $P = 1$ corresponding to pure capacitance and $P < 1$ indicating distributed relaxation time constants [73]. Nonlinear least-squares fitting of the experimental Argand diagrams yielded circuit parameters that exhibited systematic concentration-dependent trends. Non-linear least-squares fitting of the experimental Argand diagrams yielded circuit parameters that exhibited systematic concentration-dependent trends. Table 5 presents the extracted equivalent circuit parameters for all ZnO-@ doped GFRC compositions, revealing quantitative relationships between dopant concentration and interfacial electrical properties.

As evident from Table 5, the grain boundary resistance demonstrated a progressive enhancement from $R_{GB} = 2.8$ MΩ (reference) to 5.8 MΩ (2% ZnO-@), reflecting intensified interfacial charge blocking effects attributed to the formation of a ZnO nanoparticle-induced barrier layer at the cement matrix interfaces. The extracted CPE exponent values ranged from $P = 0.77$ to 0.84 across all compositions, substantiating a significant departure from the ideal capacitive response. This non-ideality arises from the inherent complexity of cementitious composites, which encompasses hierarchical pore network distributions (ranging from nanoscale C–S–H gel pores to microscale capillary pores), spatial compositional gradients between cement phases and ZnO dopants, interfacial roughness at fiber-matrix and particle–matrix boundaries, and tortuosity effects in charge carrier pathways [74, 75]. The reduced P values for optimally doped samples ($P \approx 0.77$ for 2% ZnO-@) further indicate that enhanced microstructural heterogeneity is introduced by ZnO nanoparticle dispersion, resulting in broadened relaxation time distributions and increased interfacial complexity, which is conducive to charge accumulation and dielectric loss enhancement. The obtained mechanism can be explained as Maxwell–Wagner-Sillars Interfacial Polarization, the pronounced M″ enhancement in 1–2% ZnO-@ samples originates from Maxwell–Wagner-Sillars (MWS) interfacial polarization at ZnO nanoparticle-matrix boundaries [76, 77]. The semiconducting ZnO particles (bandgap ~ 3.37 eV) embedded within the semi-insulating cement matrix create heterogeneous dielectric interfaces that accumulate space charges under applied electric fields. The characteristic relaxation time (τ = Rgb × Ceff) increased from 8.5×10^{-4} to 15.8×10^{-4} s with optimal doping, confirming enhanced charge trapping at interfacial states [78, 79]. This behavior is consistent with the Koops phenomenological model for polycrystalline dielectrics, where highly resistive grain boundaries impede charge carrier migration, resulting in elevated interfacial polarization [80–82]. Regarding the Critical Concentration Threshold and Percolation Effects, the anomalous decline in M″ max for 3% ZnO-@ samples signifies the onset of percolation-driven conductivity enhancement. Three synergistic mechanisms contribute to this phenomenon: (i) formation of conductive pathways through ZnO nanoparticle agglomeration, reducing effective interfacial area and charge accumulation capacity [83, 84]; (ii) particle clustering-induced microstructural defects compromising dielectric integrity [85]; and (iii) transition from capacitor-like to resistor-like behavior

Table 5 The extracted equivalent circuit parameters from impedance spectroscopy fitting for ZnO-@ doped GFRC composites

Sample	Rs (kΩ)	Rgb (MΩ)	C_{PE-T} ($\times 10^{-9}$ F)	C_{PE-P}	τ ($\times 10^{-4}$ s)	M''_{max}	M'_{peak}
Reference	1.2	2.8	4.2	0.82	8.5	0.0017	0.007
1% ZnO-@	1.5	4.5	3.8	0.79	12.2	0.0032	0.0075
2% ZnO-@	1.8	5.8	3.5	0.77	15.8	0.0034	0.0095
3% ZnO-@	2.1	3.2	4.5	0.84	9.1	0.0014	0.006

as inter-particle spacing approaches the charge carrier tunneling threshold (~ 2–5 nm) [86, 87]. The observed dielectric enhancement mechanisms in ZnO-@ doped GFRC composites can be rigorously understood through the framework of interfacial polarization theory applicable to heterogeneous multi-phase systems. When semiconducting ZnO nanoparticles (conductivity $\sigma_1 \approx 10^{-4}$–10^{-2} S/cm) are embedded within the semi-insulating cementitious matrix (conductivity $\sigma_2 \approx 10^{-8}$–10^{-6} S/cm), substantial conductivity and permittivity mismatches arise at phase boundaries, creating conditions favorable for Maxwell–Wagner-Sillars (MWS) interfacial polarization [18, 19]. Under applied alternating electric fields, mobile charge carriers (electrons and holes in ZnO; ionic species in the cement pore solution) migrate toward interfaces but cannot freely traverse the high-resistance boundaries, resulting in space charge accumulation and associated polarization. The characteristic relaxation time for this process, given by $\tau MWS = \varepsilon_0(\varepsilon_1 + \varepsilon_2)/(\sigma_1 + \sigma_2)$, explains why our observed relaxation frequencies (100–200 Hz) correspond to the interfacial polarization regime rather than dipolar or electronic mechanisms [76, 77]. This behavior parallels recent findings in rare-earth doped oxide composites, where similar heterogeneous interfaces generate enhanced dielectric responses through controlled defect engineering and interface density optimization [18]. The synergistic contribution of multiple polarization mechanisms, including dipolar reorientation of surface hydroxyl groups, ionic displacement polarization within the C–S–H gel structure, and predominantly MWS interfacial polarization at ZnO-cement boundaries, collectively accounts for the substantial permittivity enhancement observed in optimally doped samples. The non-monotonic concentration dependence further reflects the competing effects between increased interfacial area (beneficial for polarization) and nanoparticle agglomeration-induced conductive pathway formation (detrimental to dielectric performance), consistent with percolation theory predictions for conductive filler-insulating matrix composites [19].

The leftward centroid shift (M′ peak = 0.0095 to 0.0060) and reduced Rgb (5.8 to 3.2 MΩ) substantiate the enhanced DC conductivity, which suppresses capacitive charge storage mechanisms [88, 89]. This percolation-induced transition from dielectric-to-conductive behavior aligns with established theoretical frameworks for composite materials, where the critical percolation threshold (φc) depends on filler geometry,

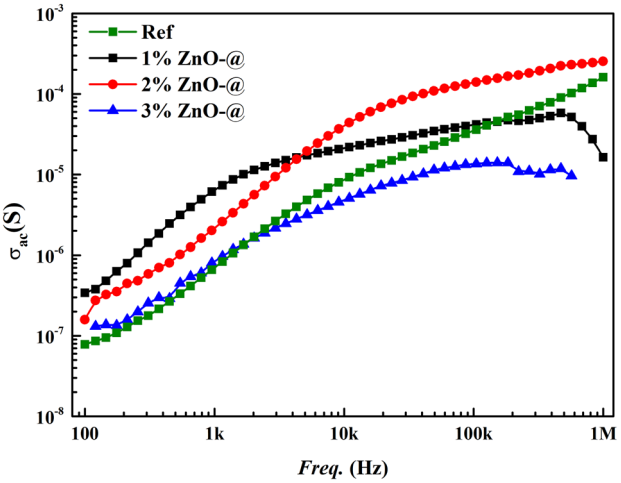

Fig. 10 The AC electrical conductivity plots of ZnO-doped GFRC composites

dispersion quality, and interfacial contact resistance. Our experimental identification of φc between 2 and 3% ZnO-@ concentration suggests that the high aspect ratio ZnO nanostructures (as evidenced by particle size distribution analysis showing Dv(90) = 199 μm) create interconnected networks at relatively low volume fractions. Similar concentration-dependent dielectric-to-conductive transitions have been documented in hybrid filler systems incorporating 2D nanomaterials and metal oxide nanoparticles, where engineered interfaces enable precise control over charge transport pathways while maintaining structural integrity [19].

Overall, the apparent contradiction between Cole–Cole (decreasing semicircle dimensions) and Argand (initial M″ enhancement) plots resolves through recognition of their complementary nature. The permittivity formalism (ε″ vs ε′) emphasizes low-frequency polarization losses and overall polarizability, whereas electric modulus (M″ vs M′) accentuates high-frequency resistive processes and localized charge transport [90, 91]. The systematic ε″ reduction (Fig. 10a) reflects diminished bulk polarizability due to ZnO's lower relative permittivity (εr ≈ 8.5) compared to hydrated cement phases (εr ≈ 10–20) [92]. Conversely, M″ enhancement indicates the creation of high-density interfacial polarization sites despite an overall reduction in polarizability, demonstrating that ZnO doping generates localized charge accumulation zones rather than bulk polarization enhancement [93, 94].

For the microstructural-dielectric property correlations, the optimal 2% ZnO-@ formulation achieves an ideal microstructural architecture, wherein semi-insulating ZnO nanoparticles establish a percolating network of interfacial polarization zones without forming continuous conductive pathways. This configuration maximizes space charge accumulation (elevated M″) while maintaining high resistivity (large Rgb), creating potential wells that trap charge carriers at interfaces [95, 96]. The interfacial layer thickness, estimated from the Debye screening length ($\lambda D = \sqrt{(\varepsilon\varepsilon_o kT/2e^2 n)} \approx 5$–$15$ nm for cementitious systems), suggests that optimal nanoparticle dispersion maintains an inter-particle spacing sufficient to prevent electron hopping while maximizing interface density [97, 98]. Furthermore, the enhanced dielectric loss tangent ($\tan\delta = M''/M'$) for 2% ZnO-@ composites translates to superior microwave absorption capacity through interfacial polarization losses and multiple scattering at heterogeneous boundaries [99, 100]. The frequency-dependent relaxation (characteristic frequency $fc = 1/2\pi\tau \approx 100$–$200$ Hz) positions these materials favorably for low-frequency EMI shielding applications in construction sectors requiring electromagnetic compatibility [101]. Conversely, the 3% ZnO-@ formulation, which exhibits suppressed relaxation losses while maintaining GFRC mechanical reinforcement, is suitable for low-loss dielectric applications, such as insulative substrates for embedded wireless communication systems [102, 103]. The successful equivalent circuit fitting validates the applicability of interfacial polarization theory to ZnO-doped GFRC composites. The non-ideal Debye behavior necessitates consideration of distributed relaxation time models (Havriliak-Negami, Cole-Davidson functions) for comprehensive frequency-domain characterization [104, 105]. The obtained CPE parameters align with reports for heterogeneous cementitious systems, where textural heterogeneity, pore size distribution, and interfacial roughness collectively generate multi-scale relaxation processes [106, 107]. On the other hand, AC conductivity (σ_{ac}) of ZnO-@ doped GFRC composites was calculated from the imaginary permittivity according to Eq. (7) as below:

$$\sigma_{ac} = \varepsilon'' \omega \varepsilon_0 \tag{7}$$

where σ_{ac} is the ac conductivity, defined as a function of ε″ and frequency, ω, denoting angular frequency equal to 2πf. The AC electrical conductivity (σ_{ac}) of ZnO-doped GFRC composite samples, compared to the control (Ref), is also revealed and presented in Fig. 10 against frequency (Hz). Both plots were on logarithmic scales. The frequency range spans from 100 Hz to 1 MHz. Conductivity of all samples increases with frequency, characteristic of AC transport in composite materials. The reference sample (Ref) exhibits the lowest conductivity across most of the frequency spectrum, indicating that ZnO doping generally enhances the electrical conductivity of GFRC composite. Among the ZnO-doped samples, the 2% ZnO concentration exhibits the highest conductivity, particularly at frequencies above 10 kHz. This suggests an optimal doping level for maximizing electrical conductivity. The 1% ZnO sample exhibits intermediate conductivity, higher than the reference but lower than the 2% ZnO sample for most of the frequency range. Interestingly, the 3% ZnO sample exhibits lower conductivity than both the 1% and 2% ZnO samples, especially at higher frequencies. This unexpected behavior might be attributed to agglomeration effects or changes in the GFRC's microstructure at higher doping concentrations. A notable feature is the sharp decrease in conductivity for the 1% ZnO sample at frequencies approaching 1 MHz, which is not observed in the other samples. This could indicate a unique frequency-dependent response mechanism in the 1% ZnO-doped GFRC composite at high frequencies. In summary, ZnO doping has a significant influence on the AC electrical conductivity of GFRC composite, with a 2% concentration providing the most substantial enhancement. The non-linear relationship between ZnO concentration and conductivity highlights the complex interactions within the composite material and underscores the importance of optimizing doping levels for specific applications.

Lastly, Fig. 11a shows the changes of real impedance (Z′) measured in megaohms (MΩ) over frequency ranging from 100 Hz to 1 MHz for ZnO-@ composite-doped GFRC composite with different ratios of added nanoparticles compared to the control sample. At the same time, the complex impedance (Z*) in Eq. 8, real and imaginary impedance (Z′ and Z″) in Eqs. 9 and 10, were identified using the following formulas:

$$Z^* = \frac{1}{i\omega C_0 \varepsilon^*} = Z' + jZ'' \tag{8}$$

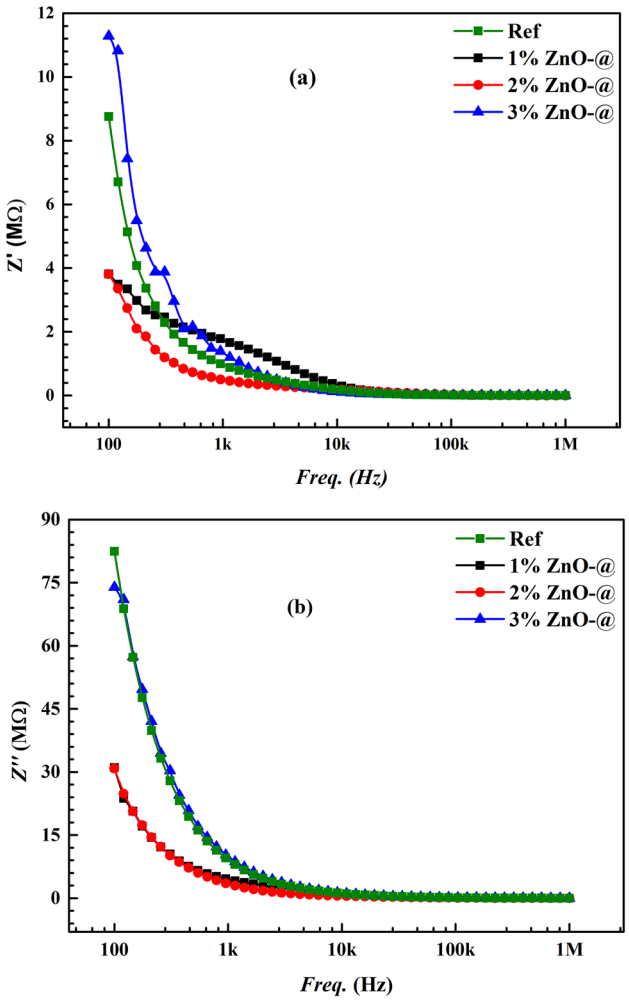

Fig. 11 **a** The real part of impedance (Z′) **b** The imaginary part of impedance (Z″) of ZnO-@ doped GFRC composite samples

$$Z' = \frac{\varepsilon''}{\omega C_o\left[\varepsilon'^2 + \varepsilon''^2\right]} \tag{9}$$

$$Z'' = \frac{\varepsilon'}{\omega C_0[\varepsilon'^2 + \varepsilon''^2]} \tag{10}$$

The results demonstrate that the impedance decreases with increasing frequency for all samples which is consistent with capacitive behavior in cementitious composites, that indicative of a capacitive nature in the materials, where impedance inversely correlates with frequency. The presence of ZnO nanoparticles significantly influences the impedance values, particularly at lower frequencies. The Reference Sample (Ref) exhibited the highest impedance across most of the frequency range, starting at approximately 10 MΩ at 100 Hz and decreasing sharply to below 2 MΩ at 1 MHz. The introduction of 1% ZnO nanoparticles results in a noticeable decrease in impedance compared to the reference. Starting just below 10 MΩ at 100 Hz, the curve follows a steep decline, closely mirroring the reference sample but maintaining consistently lower values across all frequencies. While increasing the ZnO concentration to 2% leads to a further reduction in impedance. The curve starts at around 8 MΩ at 100 Hz and decreases more rapidly than the 1% ZnO sample, indicating enhanced conductive properties due to the higher nanoparticle content. The sample with the highest concentration of ZnO shows the lowest impedance values, starting around 6 MΩ at 100 Hz. The rapid decrease in impedance is more pronounced, suggesting that the addition of more nanoparticles significantly enhances the conductivity of the GFRC. Our observations clearly demonstrate that the doping of ZnO nanoparticles into GFRC significantly affects its electrical properties, particularly the real part of impedance (Z′). As the ZnO content increases, the impedance decreases, which could be beneficial for applications requiring materials with lower electrical resistance. This behavior is likely due to the nanoparticles providing additional pathways for charge carriers, thus reducing the material's overall resistance to electrical flow. In addition, the imaginary part of impedance (Z″) was evaluated and is illustrated in Fig. 11b. Based on the observations, the impedance was found to decrease with increasing ZnO concentration, indicating enhanced conductivity. Specifically, the control sample exhibited the highest impedance across all frequencies, while the 3% ZnO-doped sample showed the lowest impedance, suggesting improved electrical connectivity. This, after all, highlights the potential of ZnO doping to modify the electrical properties of GFRC composite, making it suitable for applications requiring lower impedance and enhanced conductivity.

4 Conclusion

This systematic investigation establishes ZnO nanoparticle doping as an effective strategy for engineering multifunctional GFRC composites with enhanced dielectric and mechanical properties. The concentration-dependent dielectric response reveals complex interfacial phenomena governed by Maxwell–Wagner-Sillars polarization at nanoparticle-matrix boundaries. Optimal performance at 2% ZnO concentration

reflects an ideal microstructural architecture where semi-insulating nanoparticles establish high-density interfacial polarization zones without forming continuous conductive pathways. The pronounced enhancement in imaginary modulus (100% increase) and grain boundary resistance (5.8 MΩ) confirms effective charge accumulation mechanisms governed by Maxwell–Wagner-Sillars interfacial polarization at semiconducting ZnO-insulating cement boundaries, suitable for electromagnetic interference shielding applications. The critical percolation threshold, identified between 2 and 3% ZnO, provides crucial design parameters for tailoring electrical properties. Beyond this threshold, nanoparticle agglomeration initiates the formation of conductive pathways, suppressing capacitive behavior and reducing dielectric loss. This biphasic response demonstrates the necessity for precise compositional control in heterogeneous dielectric systems. Mechanical characterization validates structural integrity maintenance despite nanoparticle incorporation, with substantial post-aging hardness enhancement (171–176% increase), confirming long-term durability. The successful integration of semiconducting ZnO nanoparticles within the cementitious matrix, as verified through SEM–EDX and FTIR analysis, demonstrates the feasibility of developing construction materials with dual structural and functional capabilities. Future research should focus on intermediate concentration ranges (1.5–2.5% ZnO) for fine-tuning dielectric properties, investigating alternative synthesis routes to prevent nanoparticle agglomeration at elevated concentrations, and conducting field-scale assessments of electromagnetic shielding performance. Long-term environmental stability testing under varied thermal and humidity conditions remains essential for validating practical applicability. The demonstrated tunability of dielectric properties through controlled ZnO doping establishes a foundation for next-generation smart construction materials integrating energy efficiency, electromagnetic compatibility, and structural performance within unified composite systems. Several experimental limitations warrant consideration for comprehensive property validation. The dielectric measurements remain confined to ambient temperature conditions; systematic temperature-dependent impedance analysis across construction-relevant thermal ranges (− 20 °C to + 80 °C) is necessary to assess operational stability under environmental cycling. The characterized frequency domain (20 Hz–5 MHz) captures interfacial polarization mechanisms but excludes microwave frequencies (1–18 GHz), which are directly relevant to electromagnetic interference shielding applications, requiring vector network analyzer measurements for quantitative determination of shielding effectiveness. The identified copper oxide phase (Cu–O: 519 cm^{-1}) requires elemental quantification through inductively coupled plasma mass spectrometry and oxidation state confirmation via X-ray photoelectron spectroscopy to isolate its contribution to dielectric behavior. Our mechanical property assessment is limited to surface hardness; however, bulk structural performance demands the characterization of compressive strength, flexural modulus, and fracture toughness to ensure preservation of load-bearing capacity.

Acknowledgements

This study was supported by TÜBİTAK—2218 Postdoctoral Fellowship Project ID: 122C050.

Author contributions

DR: Methodology, Formal analysis, Investigation, Writing-review & editing. ABM: Formal analysis, Methodology, Investigation, Writing-original draft, Writing-review & editing. AS: Investigation, Formal analysis. AD: Writing-original draft, Writing-review & editing, Investigation, Formal analysis, Supervision, Conceptualization. SS: Conceptualization, Investigation, Methodology, Writing-review & editing, Supervision. MM: Methodology, Investigation.

Funding

Open access funding provided by the Scientific and Technological Research Council of Türkiye (TÜBİTAK). This study was funded by TÜBİTAK — 2218 Postdoctoral Fellowship Project ID: 122C050, and also supported byFibrobeton Inc.

Data availability

The datasets generated during and/or analyzed during the current study are available from the corresponding author on reasonable request.

Declarations

Conflict of interest The authors declare that they have no known competing financial interests or personal relationships that could have appeared to influence the work reported in this paper.

Ethical approval Not applicable.

References

1. O. Gencel, A.B. Musatat, A. Demir, A. Tozluoğlu, A. Tutuş, U. Kıllı et al., Transforming industrial byproduct to eco-friendly functional material: ground-granulated blast furnace slag reinforced paper for renewable energy storage. Sci. Total. Environ. **954**, 176616 (2024). https://doi.org/10.1016/j.scitotenv.2024.176616
2. Y. Wang, E.L. Runnerstrom, D.J. Milliron, Switchable materials for smart windows. Annu. Rev. Chem. Biomol. Eng. **7**, 283–304 (2016). https://doi.org/10.1146/annurev-chembioeng-080615-034647
3. N. Farzadnia, K.H. Khayat, Modification of nanomaterials for nanostructured cement-based materials. Nanotechnol. Civil Infrastr. (2023). https://doi.org/10.1016/B978-0-12-817832-4.00008-0
4. W. Dong, Y. Huang, B. Lehane, F. Aslani, G. Ma, Mechanical and electrical properties of concrete incorporating an iron-particle contained nano-graphite by-product. Constr. Build. Mater. **270**, 121377 (2021). https://doi.org/10.1016/j.conbuildmat.2020.121377
5. D. Ramazanoğlu, A. Subaşı, A.B. Musatat, A. Demir, S. Subaşı, M. Maraşlı, Dielectric property enhancement of glass fiber-reinforced concrete via TiO_2 nanocomposites. Structures **79**, 109444 (2025). https://doi.org/10.1016/j.istruc.2025.109444
6. D. Ramazanoğlu, A. Subaşı, A.B. Musatat, A. Demir, S. Subaşı, M. Maraşlı, Multifunctional SnO2-@ doped glass fiber-reinforced concrete: improved microstructure, mechanical, dielectric, and energy storage characteristics. Constr. Build. Mater. **476**, 141231 (2025). https://doi.org/10.1016/j.conbuildmat.2025.141231
7. D. Ramazanoğlu, S. Subaşı, M. Maraşlı, Innovative surface improvement of GFRC using hydrothermally produced Ch-TiO2-CuO nanohybrid composite additives. Constr. Build. Mater. **456**, 139280 (2024). https://doi.org/10.1016/J.CONBUILDMAT.2024.139280
8. A.C. Mohan, B. Renjanadevi, Preparation of zinc oxide nanoparticles and its characterization using scanning electron microscopy (SEM) and X-ray diffraction (XRD). Proced. Technol. **24**, 761–766 (2016). https://doi.org/10.1016/j.protcy.2016.05.078
9. V.N. Kalpana, B.A.S. Kataru, N. Sravani, T. Vigneshwari, A. Panneerselvam, V. Devi Rajeswari, Biosynthesis of zinc oxide nanoparticles using culture filtrates of *Aspergillus niger*: antimicrobial textiles and dye degradation studies. OpenNano **3**, 48–55 (2018). https://doi.org/10.1016/j.onano.2018.06.001
10. N. Bala, S. Saha, M. Chakraborty, M. Maiti, S. Das, R. Basu et al., Green synthesis of zinc oxide nanoparticles using *Hibiscus subdariffa* leaf extract: effect of temperature on synthesis, anti-bacterial activity and anti-diabetic activity. RSC Adv. **5**, 4993–5003 (2015). https://doi.org/10.1039/C4RA12784F
11. N. Matinise, X.G. Fuku, K. Kaviyarasu, N. Mayedwa, M. Maaza, ZnO nanoparticles via *Moringa oleifera* green synthesis: physical properties &; mechanism of formation. Appl. Surf. Sci. N.-Holl. **406**, 339–347 (2017). https://doi.org/10.1016/j.apsusc.2017.01.219
12. M.K. Wu, T. Ling, Y. Xie, X.G. Huang, X.W. Du, Performance comparison of dye-sensitized solar cells with different ZnO photoanodes. Semicond. Sci. Technol. **26**, 105001 (2011). https://doi.org/10.1088/0268-1242/26/10/105001
13. S. Chatterjee, I.B. Karki, Effect of photoanodes on the performance of dye-sensitized solar cells. J. Inst. Eng. **15**, 62–68 (2020). https://doi.org/10.3126/jie.v15i3.32008
14. V. Huynh Tan, Q. Pham My, L. Nguyen The, T. Huynh Thi Thien, Synthesis of ZnO material: a new approach by hydrothermal method. Sci. Technol. Dev. J. Nat. Sci. **5**, first (2020). https://doi.org/10.32508/stdjns.v5i1.963
15. M. Biçer, M. Gökçen, E. Orhan, Fabrication and photoanode performance of ZnO nanoflowers in ZnO-based dye-sensitized solar cells. Opt. Mater. **131**, 112691 (2022). https://doi.org/10.1016/j.optmat.2022.112691
16. L. You, B. Liu, H. Hua, H. Jiang, C. Yin, F. Wen, Energy storage performance of polymer-based dielectric composites with two-dimensional fillers. Nanomaterials **13**, 2842 (2023). https://doi.org/10.3390/nano13212842
17. S.K. Kundara, K. Chawla, D.K. Yadav, C. Lal, B. Tripathi, N. Jakhar, Study of structural, optical, electrical and dielectric properties of Gd-doped ZnO composites synthesized by solid state reaction method. Open J. Compos. Mater. **14**, 91–108 (2024). https://doi.org/10.4236/ojcm.2024.142007
18. Y. Qu, Y. Zhou, Y. Luo, Y. Liu, J. Ding, Y. Chen et al., Universal paradigm of ternary metacomposites with tunable epsilon-negative and epsilon-near-zero response for perfect electromagnetic shielding. Rare Met. **43**, 796–809 (2024). https://doi.org/10.1007/s12598-023-02510-x
19. Y. Qu, Y. Zhou, Q. Yang, J. Cao, Y. Liu, X. Qi et al., Lignin-derived lightweight carbon Aerogels for Tunable Epsilon-negative response. Adv. Sci. (2024). https://doi.org/10.1002/advs.202401767
20. C. Chen, L. Shen, G. Liu, Y. Cui, S. Yan, Improved energy storage performance of composite films based on linear/ferroelectric polarization characteristics. Polymers **16**, 1058 (2024). https://doi.org/10.3390/polym16081058

21. A. Muhammad, M. Sajid, M.N. Khan, M. Sheraz, A. Khalid, P. Ahmad et al., Optimization of physical and dielectric properties of Co-doped ZnO nanoparticles for low-frequency devices. PLoS ONE **18**, 287322 (2023). https://doi.org/10.1371/journal.pone.0287322
22. Y. Yuan, J. Lin, X. Wang, J. Qian, P. Zuo, Q. Zhuang, Achieving excellent dielectric and energy storage performance in core-double-shell-structured polyetherimide nanocomposites. Polymers **15**, 3088 (2023). https://doi.org/10.3390/polym15143088
23. C. Cheng, J. He, J. Zhang, Y. Yang, Study on the time-dependent mechanical properties of glass fiber reinforced cement (GRC) with fly ash or slag. Constr. Build. Mater. **217**, 128–136 (2019). https://doi.org/10.1016/j.conbuildmat.2019.05.063
24. J. Ahmad, R.A. González-Lezcano, A. Majdi, N. Ben Kahla, A.F. Deifalla, M.A. El-Shorbagy, Glass fibers reinforced concrete: overview on mechanical, durability and microstructure analysis. Materials **15**, 5111 (2022). https://doi.org/10.3390/ma15155111
25. A. Rai, Y.P. Joshi, Applications and properties of fibre reinforced concrete. J. Eng. Res. Appl. **4**, 123–131 (2014)
26. L.F. Lalinde, A. Mellado, M.V. Borrachero, J. Monzó, J. Payá, Durability of glass fiber reinforced cement (GRC) containing a high proportion of pozzolans. Appl. Sci. **12**, 3696 (2022). https://doi.org/10.3390/app12073696
27. J.N. Eiras, T. Kundu, M. Bonilla, J. Payá, Nondestructive monitoring of ageing of alkali resistant glass fiber reinforced cement (GRC). J. Nondestruct. Eval. **32**, 300–314 (2013). https://doi.org/10.1007/s10921-013-0183-y
28. I.G. Richardson, The calcium silicate hydrates. Cem. Concr. Res. **38**, 137–158 (2008). https://doi.org/10.1016/j.cemconres.2007.11.005
29. H.F.W. Taylor, *Cement chemistry* (Thomas Telford Publishing, Westminster, 1997)
30. M. Wyrzykowski, P. Lura, Controlling the coefficient of thermal expansion of cementitious materials – a new application for superabsorbent polymers. Cem. Concr. Compos. **35**, 49–58 (2013). https://doi.org/10.1016/j.cemconcomp.2012.08.010
31. A.B. Djurišić, X. Chen, Y.H. Leung, A. Man Ching Ng, ZnO nanostructures: growth, properties and applications. J. Mater. Chem. **22**, 6526 (2012). https://doi.org/10.1039/c2jm15548f
32. A. Kołodziejczak-Radzimska, T. Jesionowski, Zinc oxide—from synthesis to application: a review. Materials **7**, 2833–2881 (2014). https://doi.org/10.3390/ma7042833
33. R. Ylmén, U. Jäglid, B.-M. Steenari, I. Panas, Early hydration and setting of Portland cement monitored by IR, SEM and Vicat techniques. Cem. Concr. Res. **39**, 433–439 (2009). https://doi.org/10.1016/j.cemconres.2009.01.017
34. P. Barnes, J. Bensted, Structure and performance of cements [Internet]. CRC Press (2002). https://doi.org/10.1201/9781482295016
35. D.A. Long, Infrared and Raman characteristic group frequencies. Tables and charts George Socrates John Wiley and Sons, Ltd, Chichester, Third Edition, 2001. Price £135. J. Raman Spectrosc. **35**, 905–905 (2004). https://doi.org/10.1002/jrs.1238
36. J.L. Thomason, Glass fibre sizing: a review. Compos. Part A Appl. Sci. Manuf. **127**, 105619 (2019). https://doi.org/10.1016/j.compositesa.2019.105619
37. J. Thomason, L. Adzima, Sizing up the interphase: an insider's guide to the science of sizing. Compos. Part A Appl. Sci. Manuf. **32**, 313–321 (2001). https://doi.org/10.1016/S1359-835X(00)00124-X
38. S. Teixeira, K.M. Eblagon, F. Miranda, M.F. R. Pereira, J.L. Figueiredo, Towards controlled degradation of poly(lactic) acid in technical applications. C **7**, 42 (2021). https://doi.org/10.3390/c7020042
39. P. McMTLLAN, Structural studies of silicate glasses and melts-applications and limitations of Raman spectroscopy. Am. Mineral. **69**, 622–644 (1984)
40. I. García Lodeiro, D.E. Macphee, A. Palomo, A. Fernández-Jiménez, Effect of alkalis on fresh C–S–H gels. FTIR analysis. Cem. Concr. Res. **39**, 147–153 (2009). https://doi.org/10.1016/j.cemconres.2009.01.003
41. M. Criado, A. Palomo, A. Fernandezjimenez, Alkali activation of fly ashes. Part 1: effect of curing conditions on the carbonation of the reaction products. Fuel **84**, 2048–2054 (2005). https://doi.org/10.1016/j.fuel.2005.03.030
42. D.L.Y. Kong, J.G. Sanjayan, K. Sagoe-Crentsil, Comparative performance of geopolymers made with metakaolin and fly ash after exposure to elevated temperatures. Cem. Concr. Res. **37**, 1583–1589 (2007). https://doi.org/10.1016/j.cemconres.2007.08.021
43. M.Y.A. Mollah, W. Yu, R. Schennach, D.L. Cocke, A Fourier transform infrared spectroscopic investigation of the early hydration of Portland cement and the influence of sodium lignosulfonate. Cem. Concr. Res. **30**, 267–273 (2000). https://doi.org/10.1016/S0008-8846(99)00243-4
44. Z. Li, J.P. Baoguo Ma, Investigation of chloride diffusion for high-performance concrete containing fly ash, microsilica, and chemical admixtures. ACI Mater. J. (1999). https://doi.org/10.14359/638
45. D.L.Y. Kong, J.G. Sanjayan, Damage behavior of geopolymer composites exposed to elevated temperatures. Cem. Concr. Compos. **30**, 986–991 (2008). https://doi.org/10.1016/j.cemconcomp.2008.08.001
46. R. Cuscó, E. Alarcón-Lladó, J. Ibáñez, L. Artús, J. Jiménez, B. Wang et al., Temperature dependence of Raman scattering in ZnO. Phys. Rev. B **75**, 165202 (2007). https://doi.org/10.1103/PhysRevB.75.165202
47. C. Bundesmann, N. Ashkenov, M. Schubert, D. Spemann, T. Butz, E.M. Kaidashev et al., Raman scattering in ZnO thin films doped with Fe, Sb, Al, Ga, and Li. Appl. Phys. Lett. **83**, 1974–1976 (2003). https://doi.org/10.1063/1.1609251
48. N. Romčević, R. Kostić, B. Hadžić, M. Romčević, I. Kuryliszyn-Kudelska, W.D. Dobrowolski et al., Raman scattering from ZnO incorporating Fe nanoparticles: vibrational modes and low-frequency acoustic modes. J. Alloys Compd. **507**, 386–390 (2010). https://doi.org/10.1016/j.jallcom.2010.08.013
49. M. Sun, T. Hou, J. Zhou, L. Zhou, Z. Zhang, X. Li et al., Nanofibers with an adjustable core-sheath structure constructed from hyperbranched polyester for efficient loading of ZnO nanoparticles. ACS Appl. Nano Mater. **6**, 9707–9717 (2023). https://doi.org/10.1021/acsanm.3c01386
50. S. Al-Ariki, N.A.A. Yahya, S.A. Al-A'nsi, M.H.H. Jumali, A.N. Jannah, R. Abd-Shukor, Synthesis and comparative study on the structural and optical properties of ZnO doped with Ni and Ag nanopowders fabricated by sol gel technique. Sci. Rep. **11**, 11948 (2021). https://doi.org/10.1038/s41598-021-91439-1
51. S. Aksoy, Y. Caglar, Synthesis of Mn doped ZnO nanopowders by MW-HTS and its structural, morphological and optical characteristics. J. Alloys Compd. **781**, 929–935 (2019). https://doi.org/10.1016/j.jallcom.2018.12.101
52. F. Amani, H. Bidadi, M.A. Mohammadi, Structural and optical studies of copper doped zinc oxide thin films synthesized by co-precipitation method. Opt. Mater. **156**, 115965 (2024). https://doi.org/10.1016/j.optmat.2024.115965
53. A.M. Ilyas, J. Musah, S.W. Or, A.O. Awodugba, Precursor impurity-mediated effect in the photocatalytic activity of

precipitated zinc oxide. J. Am. Ceram. Soc. **107**, 8269–8280 (2024). https://doi.org/10.1111/jace.20062
54. U. Rehman, J. Jacob, A. Mahmood, K. Mahmood, A. Ali, A. Ashfaq et al., Modulation of secondary phases in hydrothermally grown zinc oxide nanostructures by varying the Cu dopant concentration for enhanced thermo power. J. Alloys Compd. **843**, 156081 (2020). https://doi.org/10.1016/j.jallcom.2020.156081
55. M.E. Sayed, S.S. Fouad, E. Baradács, L.I. Soliman, N.F. Osman, M. Nabil et al., Distinguish the effect of Cu additive on complex electrical (dielectric/impedance) behaviors of ZnO thin films. J. Nanopart. Res. **26**, 150 (2024). https://doi.org/10.1007/s11051-024-06057-5
56. A. Selmi, A. Fkiri, J. Bouslimi, H. Besbes, Improvement of dielectric properties of ZnO nanoparticles by Cu doping for tunable microwave devices. J. Mater. Sci. Mater. Electron. **31**, 18664–18672 (2020). https://doi.org/10.1007/s10854-020-04408-1
57. S. Rakshit, D. Maji, K.G. Mondal, T. Roy, P.C. Jana, B.S. Kar et al., Structural, optical and magnetic properties of chemically grown copper oxide nanoparticles: an insight into anticancer activities. Mater. Chem. Phys. **325**, 129794 (2024). https://doi.org/10.1016/j.matchemphys.2024.129794
58. N.M. Basith, J.J. Vijaya, L.J. Kennedy, M. Bououdina, Structural, morphological, optical, and magnetic properties of Ni-doped CuO nanostructures prepared by a rapid microwave combustion method. Mater. Sci. Semicond. Process. **17**, 110–118 (2014). https://doi.org/10.1016/j.mssp.2013.09.013
59. D. Gao, J. Zhang, J. Zhu, J. Qi, Z. Zhang, W. Sui et al., Vacancy-mediated magnetism in pure copper oxide nanoparticles. Nanoscale Res. Lett. (2010). https://doi.org/10.1007/s11671-010-9555-8
60. VHJMdos. Santos, D. Pontin, G.G.D. Ponzi, ASdeGe. Stepanha, R.B. Martel, M.K. Schütz et al., Application of fourier transform infrared spectroscopy (FTIR) coupled with multivariate regression for calcium carbonate (CaCO3) quantification in cement. Constr. Build. Mater. **313**, 125413 (2021). https://doi.org/10.1016/j.conbuildmat.2021.125413
61. Q. Qiu, A state-of-the-art review on the carbonation process in cementitious materials: fundamentals and characterization techniques. Constr. Build. Mater. **247**, 118503 (2020). https://doi.org/10.1016/j.conbuildmat.2020.118503
62. R. Zhang, D.K. Panesar, Secondary durability implications: steam cured, carbonated concrete containing limestone filler, and GGBFS. J. Build. Eng. **87**, 109036 (2024). https://doi.org/10.1016/j.jobe.2024.109036
63. C. Pesce, G.L. Pesce, M. Molinari, A. Richardson, Effects of organic additives on calcium hydroxide crystallisation during lime slaking. Cem. Concr. Res. **139**, 106254 (2021). https://doi.org/10.1016/j.cemconres.2020.106254
64. A. Subaşı, M. Emiroğlu, A. Demir, Polarization and relaxation mechanisms in glass fiber-reinforced LED-cured polyester composites incorporating graphene nanotubes. Mater. Sci. Eng. B Solid-State Mater. Adv. Technol. **295**, 116614 (2023). https://doi.org/10.1016/j.mseb.2023.116614
65. G. Ersöz Demir, Investigation on UV photoresponsivity of main electrical properties of Au/CuO-PVA/n-Si MPS type Schottky barrier diodes (SBDs). Phys. B Condens. Matter **604**, 412723 (2021). https://doi.org/10.1016/j.physb.2020.412723
66. D.C. Sinclair, A.R. West, Impedance and modulus spectroscopy of semiconducting BaTiO3 showing positive temperature coefficient of resistance. J. Appl. Phys. **66**, 3850–3856 (1989). https://doi.org/10.1063/1.344049
67. X. Huan, H. Li, Y. Song, J. Luo, C. Liu, K. Xu et al., Charge dynamics engineering sparks hetero-interfacial polarization for an ultra-efficient microwave absorber with mechanical robustness. Small (2024). https://doi.org/10.1002/smll.202306104
68. A.K. Jonscher, Dielectric relaxation in solids. J. Phys. D Appl. Phys. **32**, R57-70 (1999). https://doi.org/10.1088/0022-3727/32/14/201
69. J.R. Macdonald, W.B. Johnson, Fundamentals of impedance spectroscopy. Impedance Spectrosc. (2018). https://doi.org/10.1002/9781119381860.ch1
70. C.H. Hsu, F. Mansfeld, Technical note: concerning the conversion of the constant phase element parameter Y into a capacitance. Corrosion **57**, 747–748 (2001). https://doi.org/10.5006/1.3280607
71. S.X. Drakopoulos, J. Wu, S.M. Maguire, S. Srinivasan, K. Randazzo, E.C. Davidson et al., Polymer nanocomposites: interfacial properties and capacitive energy storage. Prog. Polym. Sci. **156**, 101870 (2024). https://doi.org/10.1016/j.progpolymsci.2024.101870
72. M. Samet, A. Kallel, A. Kallel-Elloumi, E. Drockenmuller, A. Serghei, Exchange process in the dielectric loss of molecular and macromolecular ionic conductors in the interfacial layers formed by electrode polarization effects. J. Phys. Chem. B **123**, 8532–8542 (2019). https://doi.org/10.1021/acs.jpcb.9b05837
73. B. Hirschorn, M.E. Orazem, B. Tribollet, V. Vivier, I. Frateur, M. Musiani, Determination of effective capacitance and film thickness from constant-phase-element parameters. Electrochim. Acta **55**, 6218–6227 (2010). https://doi.org/10.1016/j.electacta.2009.10.065
74. B.J. Christensen, T. Coverdale, R.A. Olson, S.J. Ford, E.J. Garboczi, H.M. Jennings et al., Impedance spectroscopy of hydrating cement-based materials: measurement, interpretation, and application. J. Am. Ceram. Soc. **77**, 2789–2804 (1994). https://doi.org/10.1111/j.1151-2916.1994.tb04507.x
75. W.J. McCarter, H.M. Taha, B. Suryanto, G. Starrs, Two-point concrete resistivity measurements: interfacial phenomena at the electrode–concrete contact zone. Meas. Sci. Technol. **26**, 085007 (2015). https://doi.org/10.1088/0957-0233/26/8/085007
76. K.W. Wagner, Erklärung der dielektrischen Nachwirkungsvorgänge auf Grund Maxwellscher Vorstellungen. Arch. Elektrotech. **2**, 371–387 (1914). https://doi.org/10.1007/BF01657322
77. R.W. Sillars, The Institution of Engineering and Technology, The properties of a dielectric containing semiconducting particles of various shapes. Inst. Electr. Eng. Proc. Sect. Inst. **12**, 139–155 (1937). https://doi.org/10.1049/pws.1937.0015
78. T. Wang, Z.-H. Chen, J.-W. Qiao, W. Qin, J.-Q. Liu, X.-Z. Wang et al., Correlating charge transfer dynamics with interfacial trap states in high-efficiency organic solar cells. ACS Appl. Mater. Interfaces **15**, 12109–12118 (2023). https://doi.org/10.1021/acsami.2c21470
79. B. Hu, T. Zhang, L. Li, H. Ning, G. Min, T. Wang et al., Revealing trapped carrier dynamics at buried interfaces in perovskite solar cells via infrared-modulated action spectroscopy with surface photovoltage detection. Adv. Mater. (2025). https://doi.org/10.1002/adma.202502160
80. C.G. Koops, American Physical Society, On the dispersion of resistivity and dielectric constant of some semiconductors at audiofrequencies. Phys. Rev. **83**, 121–124 (1951). https://doi.org/10.1103/PhysRev.83.121
81. A. Alasmari, K. Alshehri, A.A. Azab, S. Solyman, IOP Publishing, Detailed investigation of the structural and electrical

properties of ZnO/Fe 3 O 4 nanocomposites. Phys. Scr. **99**, 035921 (2024). https://doi.org/10.1088/1402-4896/ad21c9
82. C. Rayssi, S. El.Kossi, J. Dhahri, K. Khirouni, Frequency and temperature-dependence of dielectric permittivity and electric modulus studies of the solid solution Ca 0.85 Er 0.1 Ti 1−x Co 4x/3 O 3 ($0 \leq x \leq 0.1$). RSC Adv. **8**, 17139–17150 (2018). https://doi.org/10.1039/C8RA00794B
83. G. Wang, American Chemical Society, Enhanced dielectric properties of three-phase-percolative composites based on thermoplastic-ceramic matrix (BaTiO 3 + PVDF) and ZnO radial nanostructures. ACS Appl. Mater. Interfaces **2**, 1290–1293 (2010). https://doi.org/10.1021/am100296u
84. O. Oabi, A. Maaroufi, B. Lucas, Frequency electrical conductivity dependence and dielectric relaxation of ZnO–P2O5/Co composites. J. Mater. Sci. Mater. Electron. **29**, 15902–15911 (2018). https://doi.org/10.1007/s10854-018-9676-x
85. L. Padurariu, E. Brunengo, G. Canu, L.P. Curecheriu, L. Conzatti, M.T. Buscaglia et al., Role of microstructures in the dielectric properties of PVDF-based nanocomposites containing high-permittivity fillers for energy storage. ACS Appl. Mater. Interfaces **15**, 13535–13544 (2023). https://doi.org/10.1021/acsami.2c23013
86. M. Cervo Sulzbach, H. Tan, S. Estandía, J. Gàzquez, F. Sánchez, I. Fina et al., Polarization and resistive switching in epitaxial 2 nm Hf 0.5 Zr 0.5 O 2 tunnel junctions. ACS Appl. Electron. Mater. **3**, 3657–3666 (2021). https://doi.org/10.1021/acsaelm.1c00604
87. K. Pramod, R.B. Gangineni, High-voltage transition studies from rectification to resistive switching in Ag/PVDF/Au capacitor-like structures. Polym. Bull. **75**, 2769–2778 (2018). https://doi.org/10.1007/s00289-017-2178-9
88. Q. Li, H. Wang, X. Tang, M. Zhou, H. Zhao, Y. Xu et al., Electrical conductivity adjustment for interface capacitive-like storage in sodium-ion battery. Adv. Funct. Mater. (2021). https://doi.org/10.1002/adfm.202101081
89. J. Chen, J. Xue, J. Dong, Y. Li, J. Deng, G.-J. Zhang, Effects of surface conductivity on surface charging behavior of DC-GIL spacers. IEEE Trans. Dielectr. Electr. Insul. **27**, 1038–1045 (2020). https://doi.org/10.1109/TDEI.2020.008707
90. S. Sinha, S.K. Chatterjee, J. Ghosh, A.K. Meikap, Analysis of the dielectric relaxation and ac conductivity behavior of polyvinyl alcohol-cadmium selenide nanocomposite films. Polym. Compos. **38**, 287–298 (2017). https://doi.org/10.1002/pc.23586
91. J. Saji, A. Khare, S.P. Mahapatra, Relaxation behavior of nanographite-reinforced silicon elastomer nanocomposites. High Perform. Polym. **28**, 3–13 (2016). https://doi.org/10.1177/0954008314568729
92. K.-P. Kunal, A.E. N., Examination of chloride-induced corrosion in reinforced geopolymer concretes. J. Mater. Civ. Eng. **25**, 1465–1476 (2013). https://doi.org/10.1061/(ASCE)MT.1943-5533.0000672
93. G.C. Psarras, Hopping conductivity in polymer matrix–metal particles composites. Compos. Part A Appl. Sci. Manuf. **37**, 1545–1553 (2006). https://doi.org/10.1016/j.compositesa.2005.11.004
94. Y.V. Gomeniuk, P.M. Lytvyn, Y.Y. Gomeniuk, T.E. Rudenko, A.V. Vasin, A.V. Rusavsky et al., Charge transport and charge trapping in polycrystalline ZnO thin films doped by methane: local and integrated analysis. Phys. Scr. **100**, 025905 (2025). https://doi.org/10.1088/1402-4896/ada4ea
95. J. Cao, D.D. Chung, Electric polarization and depolarization in cement-based materials, studied by apparent electrical resistance measurement. Cem. Concr. Res. **34**, 481–485 (2004). https://doi.org/10.1016/j.cemconres.2003.09.003
96. P. Xie, P. Gu, J.J. Beaudoin, Electrical percolation phenomena in cement composites containing conductive fibres. J. Mater. Sci. **31**, 4093–4097 (1996). https://doi.org/10.1007/BF00352673
97. F. Sanchez, K. Sobolev, Nanotechnology in concrete – a review. Constr. Build. Mater. Elsevier **24**, 2060–2071 (2010). https://doi.org/10.1016/j.conbuildmat.2010.03.014
98. A.M. Smith, A.A. Lee, S. Perkin, The electrostatic screening length in concentrated electrolytes increases with concentration. J. Phys. Chem. Lett. **7**, 2157–2163 (2016). https://doi.org/10.1021/acs.j.pclett.6b00867
99. G. Wang, C. Li, D. Estevez, P. Xu, M. Peng, H. Wei et al., Boosting interfacial polarization through heterointerface engineering in MXene/graphene intercalated-based microspheres for electromagnetic wave absorption. Nano-Micro Lett. **15**, 152 (2023). https://doi.org/10.1007/s40820-023-01123-4
100. Z. Wu, C. Jin, Z. Yang, R. Che, Integrating hierarchical interfacial polarization in yeast-derived Mo2C/C nanoflower/microsphere nanoarchitecture for boosting microwave absorption performance. Carbon **189**, 530–538 (2022). https://doi.org/10.1016/j.carbon.2021.12.073
101. J. Cao, D.D.L. Chung, Improving the dispersion of steel fibers in cement mortar by the addition of silane. Cem. Concr. Res. **31**, 309–311 (2001). https://doi.org/10.1016/S0008-8846(00)00470-1
102. M.T. Sebastian, R. Ubic, H. Jantunen, Low-loss dielectric ceramic materials and their properties. Int. Mater. Rev. **60**, 392–412 (2015). https://doi.org/10.1179/1743280415Y.0000000007
103. H. Srinivasa Varaprasad, P.V. Sridevi, M. Satya Anuradha, Optical, morphological, electrical properties of ZnO-TiO2-SnO2/CeO2 semiconducting ternary nanocomposite. Adv. Powder Technol. **32**, 1472–1480 (2021). https://doi.org/10.1016/j.apt.2021.02.042
104. G.M. Tsangaris, G.C. Psarras, N. Kouloumbi, Electric modulus and interfacial polarization in composite polymeric systems. J. Mater. Sci. **33**, 2027–2037 (1998). https://doi.org/10.1023/A:1004398514901
105. A.N. Asokan, A.P. Anagha, P. Preetha, K. Sunitha, Effect of interphase on dielectric relaxation mechanisms in epoxy-alumina nanocomposite. IEEE Trans. Dielectr. Electr. Insul. **26**, 1211–1219 (2019). https://doi.org/10.1109/TDEI.2019.007960
106. F. Rajabipour, J. Weiss, Electrical conductivity of drying cement paste. Mater. Struct. **40**, 1143–1160 (2007). https://doi.org/10.1617/s11527-006-9211-z
107. F. He, R. Wang, C. Shi, R. Zhang, C. Chen, L. Lin et al., Differential analysis of AC impedance spectroscopy of cement-based materials considering CPE behavior. Constr. Build. Mater. **143**, 179–188 (2017). https://doi.org/10.1016/j.conbuildmat.2017.03.119